Shear Horizontal Surface Acoustic Wave Microsensor for Class A Viral and Bacterial Detection

Darren W. Branch, Thayne L. Edwards, Dale Huber, and Susan M. Brozik

Sandia National Laboratories

Shear Horizontal Surface Acoustic Wave Microsensor for Class A Viral and Bacterial Detection

Darren W. Branch, Thayne L. Edwards, Dale Huber, and Susan M. Brozik

Biosensor and Nanomaterials Department
Sandia National Laboratories
PO Box 5800
Albuquerque, NM 87185-1425

ABSTRACT

The rapid autonomous detection of pathogenic microorganisms and bioagents by field deployable platforms is critical to human health and safety. To achieve a high level of sensitivity for fluidic detection applications, we have developed a 330 MHz Love wave acoustic biosensor on 36° YX Lithium Tantalate (LTO). Each die has four delay-line detection channels, permitting simultaneous measurement of multiple analytes or for parallel detection of single analyte containing samples. Crucial to our biosensor was the development of a transducer that excites the shear horizontal (SH) mode, through optimization of the transducer, minimizing propagation losses and reducing undesirable modes. Detection was achieved by comparing the reference phase of an input signal to the phase shift from the biosensor using an integrated electronic multi-readout system connected to a laptop computer or PDA. The Love wave acoustic arrays were centered at 330 MHz, shifting to 325-328 MHz after application of the silicon dioxide waveguides. The insertion loss was −6 dB with an out-of-band rejection of 35 dB. The amplitude and phase ripple were 2.5 dB p-p and 2-3° p-p, respectively. Time-domain gating confirmed propagation of the SH mode while showing suppression of the triple transit. Antigen capture and mass detection experiments demonstrate

a sensitivity of 7.19 ± 0.74 ° mm^2 / ng with a detection limit of 6.7 ± 0.40 pg / mm^2 for each channel.

CONTENTS

1.0 INTRODUCTION

Recently, Love wave sensors have received considerable attention for their high mass and viscous sensitivity with a minimal need for additional reagents. Minimizing the use of reagents is an essential requirement for field deployable biodetection systems. The transduction mechanism for Love wave sensors is based on propagating waves with a shear-horizontal polarization (SH) along the propagation direction. The SH polarization minimizes attenuation of the surface acoustic wave (SAW) into viscous media permitting detection in fluids [1-4].

Love wave sensors are comprised of a substrate that primarily excites SH waves, which are subsequently confined by a thin guiding layer. This waveguide layer is crucial to achieve high sensitivity by having a low shear velocity compared to the substrate [1, 5]. It also serves to provide a mechanism for stable chemical attachment through covalent linkage of antibodies, DNA, or other biomolecules to achieve the required selectivity. Waveguide materials such as polymers [6], silicon dioxide (SiO_2) [7], and more recently zinc oxide (ZnO) [8] are in use. A fluid cell provides delivery of biological antigens to the sensor surface. Added mass from captured antigens perturbs the wave propagation velocity. In a delay-line configuration, the open loop operation at constant frequency provides relative phase shifts for each delay-line channel.

This work is based on the leaky SH-type wave propagating on 36° Y-cut lithium tantalate (LTO) along the x-axis which exhibits strong coupling ($K^2 = 6.6\%$). The strong coupling on LTO provides advantages over substrates such as ST-Quartz where exquisite care in the fluidic packaging is required to prevent excessive wave damping and hence high insertion losses. We present an interdigital electrode (IDT) design that is capable of high frequency excitation of the SH-type wave on LTO for array operation. A theoretical and experimental analysis of the sensitivity and its reproducibility are presented. We present a method to assess waveguide performance through measuring the slope of $\angle S21(v)$ (° / MHz) as the waveguide thickness increased. Finally, an acquisition approach based on simultaneous phase measurements for each channel is presented with a demonstration of multi-analyte detection.

1.1.1 General Piezoelectric Problem and Shear-Horizontal (SH) Waves for Biosensing

The existence of a surface wave is determined by the material parameters, orientation, and boundary conditions. The piezoelectric material properties are specified by 4th rank elastic stiffness tensor (c_{ijkl}), 3rd rank piezoelectric tensor (e_{kij}), 2nd rank permittivity tensor (ε_{ik}), and the density (ρ) (Appendix A). The boundary conditions require that the particle displacements and traction components of stress (T_{13}, T_{23}, T_{33}) are continuous across an interface or set to zero for stress free conditions at the interface. The electrical boundary conditions are provided by the continuity of the potential and the normal component of the electric displacement across both the interface and free surface. All total there are twelve boundary conditions per layer for a general problem.

Despite the complexity of the general problem some key insights can be gained by examining the physically behavior of the free surface condition. For example, atoms at the free surface have no neighbors from one side, which results in decreased bonding to the crystal lattice. The surface layer in the material is then less rigid with regard to mechanical displacements normal to the surface such as shear vertical (SV) waves. In this manner SV waves would have a slower velocity than propagating bulk waves. However, SV waves do not satisfy stress-free boundary conditions and therefore cannot propagate along the free surface of a solid. Instead the boundary conditions dictate that SV waves must be combined with longitudinal waves, resulting in Rayleigh waves. This type of surface acoustic wave (SAW) was described by Lord Rayleigh in 1885 [9]. Unlike SV waves, shear horizontal bulk acoustic waves can satisfy stress-free boundary conditions and may propagate along a free surface. Shear horizontal (SH) is when the plane wave polarization is parallel to the surface. For a surface wave, the boundary conditions determine whether the SH wave will be confined along the surface or whether it leaks into the substrate. Recently several substrates have been discovered that support pure shear waves known as Bleustein-Gulyaev-Shimizu (BGS or pure SH) in Table 1. Pure SH modes propagate with minimal energy coupling into the substrate and external fluid media. Since these substrates are not presently used for commercial SAW devices, their application has been limited to scientific research. At present only a few manufacturers produce LGT and LGS substrates where the wafer diameter is limited to roughly 25-50mm, ruling out their use for commercial applications. For this

reason lithium tantalate (LTO) and rotated Y-cut quartz have remained the primary material for leaky SAW propagation despite their higher temperature coefficient factors (TCF).

Table 1 Several Piezoelectric Substrates that Support SSBW and SH mode Propagation

Material	Cut or Class	Euler Angle	Velocity (m/s)				K^2 (%)
			Open	**Wave**	**Short**	**Wave**	
[1]LTO	36° YX	(0°,-54°,0°)	4177	SSBW	4077	SH	7.0
[2]KNO		(0°,90°,0°)	4500	SH	4425	SH	5.3
[3]Quartz	Rotated Y (ST)	(0°,132.75°,90°)	4993.5	SSBW	4993	SH	-
[3]Quartz	35.5° (AT)	(0°,125.5°,90°)	5093.2	SH	5093.2	SH	-
[4]Quartz	36° YZ	(0°,54.2°,90°)	4212	SSBW	4160	SH	4.7
[5]LGT	(0°,θ,90°)	(0°,69.8°,90°)	3070	SH		SH	
		(0°,132°,90°)	2280	SH		SH	
[6]LGS	(0°,θ,90°)	(0°,22°,90°)	2790	SH		SH	

[1] lithium tantalate [10] calculated
[2] potassium niobate [11]
[3] [12]
[4] calculated
[5] LGT: Langatate ($La_3Ga_{5.5}Ta_{0.5}O_{14}$) [13, 14]
[6] LGS: Langasite ($La_3Ga_5 SiO_{14}$) [15]

1.1.2 Shear Horizontal Biosensors

To obtain optimum performance for Love wave sensors, it is essential to provide proper electrical shielding of the transducers and sensing regions (e.g. delay line) from the dielectric perturbation due to the fluid. For detection of changes in mechanical properties (i.e. from a thin biological film), electrical perturbations must be kept at a minimum. Dielectric properties of fluids, namely buffers carrying ionic species can cause significant changes in the capacitance and hence admittance of the interdigital transducer (IDT) unless properly isolated. Confining the fluid between the IDTs is one approach to reduce electrical perturbations from large variations in the external permittivity. There are three strategies to reduce changes in IDT admittance: 1) confine the fluid between the IDTs using a specialized flow cell, 2) deposit a dielectric insulation layer over the entire device, and 3) deposit a metal shielding layer over the isotropic guiding layer. The first two strategies are often used together, whereas adding a metalized shield is more cumbersome since it must also be grounded which adds complexity to the packaging process and the metal layer may interfere with the attachment of additional biological layers. Commercial SAW devices often use metal shields to reduce electrical feed-through between the IDTs, however this shield is designed to operate in hermetically sealed environment.

$$f_c = V_R/\lambda = V_R/2p = V_R/4a$$
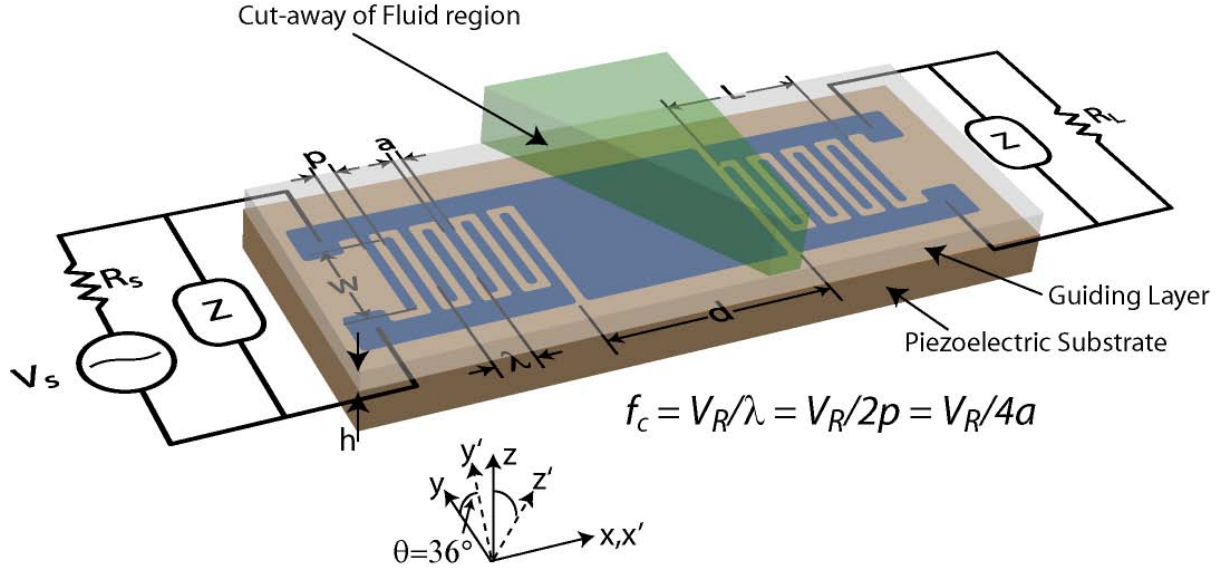
Fig. 1 Love wave biosensor on 36° YX lithium tantalate (0°,-54°, 0°). The blue regions shows a simple IDT geometry having a uniform strip width *a* and periodicity *p* and a metallization ratio of 0.5 ($\eta = a/p$). In practice, the IDTs are often far more complex to reduce coupling between the SSBW and excitation of the longitudinal mode. The center frequency is computed from strip width and acoustic velocity for the crystal type and orientation. The IDT design is tapped uniformly and illustrates the simplest layout for launching surface acoustic waves. For leaky wave generation this design is problematic since the IDT is bidirectional and also generates a significant bulk wave component that interferes with the leaky mode propagation.

A basic SAW device known as a delay-line is shown in Fig 1. A piezoelectric substrate has a polished upper surface on which two IDTs are deposited using photolithographic methods. The left-hand input transducer is connected, via fine bonded leads, to the electric source (V_s) through an electrical matching network and source resistance, (R_s). The right-hand output transducer drives the load (R_L), usually 50 ohms, through another electrical matching network (*Z*). Recent advancements in computer modeling have led to the development of 50 ohm IDT designs that do not require external electrical matching networks. The center frequency (f_c) is governed by the Rayleigh wave velocity (V_R) on the piezoelectric substrate and the electrode width (*a*) of a single finger, according to $f_c = V_R/4a$. For SAW devices, the velocity of wave depends on the properties of the piezoelectric crystal and its crystallographic orientation. Computer models have proven essential to search through numerous crystallographic orientations to search for the existence and type of acoustic wave.

In filter applications, the width of the passband is critical for frequency selection, which is governed by length of the IDT (*L*). Increasing *L* by the addition of more electrode pairs sharpens the filter response and reduces noise. IDT-to-IDT spacing (*d*) is used to select the

10

delay-time or phase slope of the filter. The IDT aperture (*w*) governs the diffraction behavior and determines transducer output power. Owing to symmetry, each transducer generates acoustic waves equally in two opposite directions, so that it is bidirectional. In this case, half of the power is propagating in an unwanted direction, giving a loss of -3dB (i.e. $10 \cdot \log_{10}(0.50)$), and in a delay-line with two IDTs contributes to -6dB of insertion loss in the passband. For Rayleigh SAW devices, silicon rubber is a very effective absorber, reducing the amplitude of the backward traveling waves by over 30 dB. However, SAW devices that use shear-horizontal or surface skimming bulk waves are not attenuated by absorbers and therefore require unidirectional transducers. Absorber efficiency depends on the acoustic absorption properties of the material and the type of acoustic wave. By using unidirectional transducers, acoustic waves will propagate preferentially in one direction, which dramatically reduces overall acoustic loss. State-of-art SAW devices use unidirectional IDTs, eliminating the need for absorbers. Insertion losses for unidirectional transducers are around -4 dB or better, depending on the substrate type.

In biosensor applications a flow cell is essential to confine the fluid and prevent electrical breakdown at the bonding pads. In Fig. 1 the fluid (green) is confined between the IDTs by a specialized flow cell. In addition to the flow cell, a thin dielectric layer is deposited on the piezoelectric substrate to reduce changes in capacitance from the dielectric media. Later we will see that the application of the dielectric insulation layer also serves as a guiding layer to enhance sensitivity, performance, and permit chemical attachment of recognition films for specific detection applications.

1.2 THEORY

1.2.1 Generalized Green's Function and Effective Permittivity

The design and optimization of complex interdigital transducers on a wide variety of substrates requires detailed knowledge of wave excitation and propagation. The concept of the effective permittivity introduced the idea that a specific relationship exists between the charge and the electrical potential distribution [16]. To determine the amplitude of the electric potential, the full system of piezoelectric coupled acoustic and electrostatic equations must be solved. Due to linearity of elastic media, the amplitudes of the charge and potential are fortunately proportional to each other and their ratio is independent. In the absence of

piezoelectricity, the effective permittivity reduces to the dielectric permittivity. The effective permittivity calculation takes into account generation of all possible acoustic waves propagating in the sagittal plane, excited by a charge distribution on a mechanically free surface. However, the limitation is that the effective permittivity does not address the relationship between surface stresses and charge on mechanical motion and acoustic potential. Instead, the complete description requires introduction of the 16-element Green's function, where the effective permittivity is represented by a single matrix element, G_{44}.

Calculation of the 16-element Green's function requires the use of matrix methods to change the problem from several independent steps involving determinants [17] and boundary condition matrices into a single compact eigenvalue problem [18] [19]. Once calculated, the Green's function provides a precise relationship between the acoustic stresses and electric displacement on the three mechanical displacement and electric potential. In this way, the Green's function acts as a source term for acoustic wave generation. The behavior is often highly complicated with no functional form which also depends on the type of excitation (e.g. Rayleigh). Once computed, interpolation methods can be used to capture the functional behavior by numerically sampling near the pole regions. Extending this technique permits calculation of a spatial Green's function, which can be very powerful toward analyzing acoustic wave excitation and propagation in interdigital structures [20].

Acoustic waves must satisfy both Newton's and Maxwell's equations. In the absence of external forces, the equations are expressed as

$$\rho \frac{\partial^2 u_i}{\partial t^2} = \nabla \cdot T \tag{1.1}$$

$$S = \nabla_s u \tag{1.2}$$

$$\nabla \cdot D = \rho_f \tag{1.3}$$

where ρ is the mass density, u is the particle displacement, and T and S are the surface stress and strain components, respectively. D and ρ_f are the electric displacement and free charge density, respectively. The free charge density ρ_f is zero everywhere except at the surface of the substrate.

In a piezoelectric substrate, the coupled constitutive equations for piezoelectric media are given by,

$$T_{ij} = c_{ijkl}^{E} S_{kl} - e_{kij}^{t} E_{k} \tag{1.4}$$

$$D_{i} = e_{ikl} S_{kl} + \varepsilon_{ik}^{S} E_{k} \tag{1.5}$$

where e and c^{E} are the piezoelectric stress constants and stiffness constants. Since the coupling between the electric and elastic fields is weak, the magnetic fields can be neglected and the electric fields derived from the scalar potential. This is known as the static field approximation in which the particle displacements u_{i} are along the coordinate axis x_{i}. In (1.4) and (1.5), we recognize Hooke's law and $D = \varepsilon E$, where $E = -\nabla \phi$ and ϕ is the electrical potential on the surface. By substituting (1.4) and (1.5) into (1.1) and (1.3) yields,

$$\rho \frac{\partial^{2} u}{\partial t^{2}} = \nabla \cdot c^{E} : \nabla_{s} u - \nabla \cdot (e \cdot E) \tag{1.6}$$

$$\nabla \cdot (e : \nabla_{s} u) - \nabla \cdot (\varepsilon^{s} \cdot \nabla \phi) = 0 \tag{1.7}$$

A. Traditional Method

To obtain solutions, plane wave forms are assumed for both the particle displacement and electric potential with the following forms for the piezoelectric substrate [17, 21, 22],

$$u_{i} = \left\{ \sum_{m=1}^{4} C_{m} \beta_{i}^{m} e^{\alpha^{(m)} k x_{3}} \right\} e^{j\omega\left(t - \frac{x_{1}}{v}\right)}, x_{3} < 0$$

$$\phi = \left\{ \sum_{m=1}^{4} C_{m} \beta_{4}^{m} e^{\alpha^{(m)} k x_{3}} \right\} e^{j\omega\left(t - \frac{x_{1}}{v}\right)}, x_{3} < 0 \tag{1.8}$$

The trial solutions in (1.8) vary amongst authors which changes the conditions for the allowed values of α, otherwise the solution process is identical. Substituting (1.8) into (1.6) and (1.7), gives four linear equations for particle displacement u and potential ϕ [23]

$$A \begin{bmatrix} \overline{u_{1}} \\ \overline{u_{2}} \\ \overline{u_{3}} \\ \overline{\phi} \end{bmatrix} = \left(\alpha^{2} A_{1} - j\alpha A_{2} + A_{3} \right) \begin{bmatrix} \overline{u_{1}} \\ \overline{u_{2}} \\ \overline{u_{3}} \\ \overline{\phi} \end{bmatrix} = 0 \tag{1.9}$$

where A is a second order function of α, and the bars indicate the Fourier transformation with respect to x_{1} in k-space. The coefficients of the matrix are given as

$$A_1 = \begin{bmatrix} c_{55}^E & c_{45}^E & c_{35}^E & e_{35} \\ c_{45}^E & c_{44}^E & c_{34}^E & e_{34} \\ c_{35}^E & c_{34}^E & c_{33}^E & e_{33} \\ e_{35} & e_{34} & e_{33} & -\varepsilon_{33}^S \end{bmatrix} \tag{1.10}$$

$$A_2 = \begin{bmatrix} c_{15}^E + c_{51}^E & c_{14}^E + c_{56}^E & c_{13}^E + c_{55}^E & e_{15}^E + e_{31} \\ c_{14}^E + c_{56}^E & c_{46}^E + c_{64}^E & c_{36}^E + c_{45}^E & e_{14}^E + e_{36} \\ c_{13}^E + c_{55}^E & c_{36}^E + c_{45}^E & c_{35}^E + c_{53}^E & e_{13}^E + e_{35} \\ e_{15}^E + e_{31} & e_{14}^E + e_{36} & e_{13}^E + e_{35} & -\varepsilon_{13}^S - \varepsilon_{31}^S \end{bmatrix} \tag{1.11}$$

$$A_3 = \begin{bmatrix} -c_{11}^E + \rho v^2 & -c_{16}^E & -c_{15}^E & -e_{11} \\ -c_{16}^E & -c_{66}^E + \rho v^2 & -c_{56}^E & -e_{16} \\ -c_{15}^E & -c_{56}^E & -c_{55}^E + \rho v^2 & -e_{15} \\ -e_{11} & -e_{16} & -e_{15} & \varepsilon_{11} \end{bmatrix} \tag{1.12}$$

where $v = \omega / k$ is the phase velocity along the x_1 direction. For non-trivial solution of (1.9) the determinant of the coefficient matrix A must be zero for each value of v, which leads to an 8th order polynomial in α. Bounded solutions in (1.8) further require the $\Box \left\{ k\alpha^{(m)} \right\} > 0$ to eliminate solutions that increase with depth into the substrate. For each valid root $\alpha^{(m)}$, we obtain four eigenvectors $\beta_i^{(m)} \to \beta_1^1, \beta_2^1, \beta_3^1, \beta_4^1$ and thus a partial wave solution. The solution of the system of linear equations is a linear combination of these partial solutions normalized by ϕ given as

$$\begin{bmatrix} \overline{u_1} \\ \overline{u_2} \\ \overline{u_3} \\ \overline{\phi} \end{bmatrix} = \begin{bmatrix} \beta_1^{(1)} & \beta_1^{(2)} & \beta_1^{(3)} & \beta_1^{(4)} \\ \beta_2^{(1)} & \beta_2^{(2)} & \beta_2^{(3)} & \beta_2^{(4)} \\ \beta_3^{(1)} & \beta_3^{(2)} & \beta_3^{(3)} & \beta_3^{(4)} \\ 1 & 1 & 1 & 1 \end{bmatrix} \begin{bmatrix} C_1 e^{\alpha^{(1)} k x_3} \\ C_2 e^{\alpha^{(2)} k x_3} \\ C_3 e^{\alpha^{(3)} k x_3} \\ C_4 e^{\alpha^{(4)} k x_3} \end{bmatrix} \tag{1.13}$$

The stresses and electrical displacement are obtained by substituting (1.13) into (1.4) and (1.5)

$$
\begin{bmatrix} \overline{T_{13}} \\ \overline{T_{23}} \\ \overline{T_{33}} \\ \overline{D_3} \end{bmatrix} = \begin{bmatrix} \overline{T_{13}^{(1)}} & \overline{T_{13}^{(2)}} & \overline{T_{13}^{(3)}} & \overline{T_{13}^{(4)}} \\ \overline{T_{23}^{(1)}} & \overline{T_{23}^{(2)}} & \overline{T_{23}^{(3)}} & \overline{T_{23}^{(4)}} \\ \overline{T_{33}^{(1)}} & \overline{T_{33}^{(2)}} & \overline{T_{33}^{(3)}} & \overline{T_{33}^{(4)}} \\ \overline{D_3^{(1)}} & \overline{D_3^{(2)}} & \overline{D_3^{(3)}} & \overline{D_3^{(4)}} \end{bmatrix} \begin{bmatrix} C_1 e^{\alpha^{(1)} k x_3} \\ C_2 e^{\alpha^{(2)} k x_3} \\ C_3 e^{\alpha^{(3)} k x_3} \\ C_4 e^{\alpha^{(4)} k x_3} \end{bmatrix}
\tag{1.14}
$$

where

$$
\begin{bmatrix} \overline{T_{13}^{(i)}} \\ \overline{T_{23}^{(i)}} \\ \overline{T_{33}^{(i)}} \\ \overline{D_3^{(i)}} \end{bmatrix} = k \left(\alpha^{(i)} A_1 - j A_4 \right) \begin{bmatrix} \overline{u_1^{(i)}} \\ \overline{u_2^{(i)}} \\ \overline{u_3^{(i)}} \\ 1 \end{bmatrix}, i \rightarrow 1...4
\tag{1.15}
$$

$$
A_4 = \begin{bmatrix} c_{15}^E & c_{56}^E & c_{55}^E & e_{15} \\ c_{14}^E & c_{46}^E & c_{45}^E & e_{14} \\ c_{13}^E & c_{36}^E & c_{35}^E & e_{13} \\ e_{31} & e_{36} & e_{35} & -\varepsilon_{13}^s \end{bmatrix}
\tag{1.16}
$$

Boundary Conditions

The coefficients C_m are determined from application of the boundary conditions, requiring stress free conditions at the free surface $x_3 = 0$,

$$
T_{13}(x_1, 0) = T_{23}(x_1, 0) = T_{33}(x_1, 0) = 0
\tag{1.17}
$$

Additional layers require continuity of stresses and displacement with 12 boundary conditions per for piezoelectric layers. For the electric displacement D the normal component must be continuous across the boundary at $x_3 = 0$. Inside the piezoelectric substrate the electric displacement is given by

$$
D_3(x_1, 0^-) = e_{3kl} \frac{\partial u_k}{\partial x_l} - \varepsilon_{3k} \frac{\partial \phi}{\partial x_k}
\tag{1.18}
$$

In the vacuum above the substrate ($x_3 > 0$), the electrical potential must satisfy Laplace's equation

$$
\nabla^2 \phi = \frac{\partial^2 \phi}{\partial x_1^2} + \frac{\partial^2 \phi}{\partial x_3^2} = 0
\tag{1.19}
$$

Because ϕ is proportional to e^{-jkx_1} and must vanish at $x_3 \rightarrow \infty$, the x_3 dependence is $e^{-|k|x_3}$ for $x_3 > 0$. For each solution of $\alpha^{(m)}$, there is one corresponding partial wave solution of the potential for $x_3 > 0$, and the potential must be continuous across the free surface giving,

$$\phi(x_1, x_3 > 0) = \sum_{m=1}^{4} C_m e^{-jkx_1 - |k|x_3} \tag{1.20}$$

Therefore,

$$D_3(x_1, 0^+) = -\varepsilon_0 \frac{\partial \phi}{\partial x_3} = \varepsilon_0 k \sum_{m=1}^{4} C_m e^{-jkx_1} \tag{1.21}$$

The electrical boundary condition at $x_3=0$ surface is

$$D_3(x_1, 0^+) - D_3(x_1, 0^-) = \sigma(x_1) \tag{1.22}$$

where σ is the surface charge density. The surface potential $\phi(x_1, 0)$ must be the same on both sides of the boundary however the normal components of the electrical displacement can differ. The discontinuity is related to the potential by the effective permittivity $\varepsilon_s(k)$ as

$$\varepsilon_s(k) = \frac{\overline{D_3}(k)\big|_{x_3=0^+} - \overline{D_3}(k)\big|_{x_3=0^-}}{|k| \cdot \overline{\phi}(k)} = \frac{\overline{\sigma}(k)}{|k| \cdot \overline{\phi}(k)} \tag{1.23}$$

The Green's function is defined as the potential excited by a line source with free charge density, such that

$$\phi(x_1, 0) = G_{44}(x_1, 0) * \sigma(x_1, 0) \tag{1.24}$$

In the absence of surface stresses, this expression fully describes the behavior of acoustic waves when the electrical boundary conditions are applied. The two electrical conditions considered are zero charge on un-metalized surface regions (open-condition) and constant potential on metalized surface regions (short-condition). Applying the Fourier transformation with respect to x_1 on both sides of (1.24) gives an expression in the k domain,

$$\overline{G_{44}}(k) = \frac{\overline{\phi}(k)}{\overline{\sigma}(k)} \tag{1.25}$$

Therefore the effective permittivity can be determined using,

$$\varepsilon_s(k) = \frac{\overline{\sigma}(k)}{|k|\overline{\phi}(k)} = \frac{1}{k \cdot \overline{G}_{44}(k)} \tag{1.26}$$

B. Generalized Method

In the general Green's function approach the vector $\begin{bmatrix} \overline{T}_{13} & \overline{T}_{23} & \overline{T}_{33} & \overline{D}_3' \end{bmatrix}$ is defined as the exciting source. The Green's function can be expressed as

$$\overline{G} = \begin{bmatrix} \beta_1^{(1)} & \beta_1^{(2)} & \beta_1^{(3)} & \beta_1^{(4)} \\ \beta_2^{(1)} & \beta_2^{(2)} & \beta_2^{(3)} & \beta_2^{(4)} \\ \beta_3^{(1)} & \beta_3^{(2)} & \beta_3^{(3)} & \beta_3^{(4)} \\ 1 & 1 & 1 & 1 \end{bmatrix} \begin{bmatrix} C_1 \\ C_2 \\ C_3 \\ C_4 \end{bmatrix} \begin{bmatrix} \overline{T_{13}^{(1)}} & \overline{T_{13}^{(2)}} & \overline{T_{13}^{(3)}} & \overline{T_{13}^{(4)}} \\ \overline{T_{23}^{(1)}} & \overline{T_{23}^{(2)}} & \overline{T_{23}^{(3)}} & \overline{T_{23}^{(4)}} \\ \overline{T_{33}^{(1)}} & \overline{T_{33}^{(2)}} & \overline{T_{33}^{(3)}} & \overline{T_{33}^{(4)}} \\ \overline{D_3^{(1)\prime}} & \overline{D_3^{(2)\prime}} & \overline{D_3^{(3)\prime}} & \overline{D_3^{(4)\prime}} \end{bmatrix}^{-1} \Bigg|_{x_3=0} \tag{1.27}$$

Setting $\overline{u}_i(x_3 = 0) = \sum\limits_{m=1}^{4} C_m \beta_i^m, i \to 1...4$ gives

$$\overline{G} = \begin{bmatrix} \overline{u_1^{(1)}} & \overline{u_1^{(2)}} & \overline{u_1^{(3)}} & \overline{u_1^{(4)}} \\ \overline{u_2^{(1)}} & \overline{u_2^{(2)}} & \overline{u_2^{(3)}} & \overline{u_2^{(4)}} \\ \overline{u_3^{(1)}} & \overline{u_3^{(2)}} & \overline{u_3^{(3)}} & \overline{u_3^{(4)}} \\ 1 & 1 & 1 & 1 \end{bmatrix} \begin{bmatrix} \overline{T_{13}^{(1)}} & \overline{T_{13}^{(2)}} & \overline{T_{13}^{(3)}} & \overline{T_{13}^{(4)}} \\ \overline{T_{23}^{(1)}} & \overline{T_{23}^{(2)}} & \overline{T_{23}^{(3)}} & \overline{T_{23}^{(4)}} \\ \overline{T_{33}^{(1)}} & \overline{T_{33}^{(2)}} & \overline{T_{33}^{(3)}} & \overline{T_{33}^{(4)}} \\ \overline{D_3^{(1)\prime}} & \overline{D_3^{(2)\prime}} & \overline{D_3^{(3)\prime}} & \overline{D_3^{(4)\prime}} \end{bmatrix}^{-1} \tag{1.28}$$

and $\overline{D_3^{(i)\prime}} = \overline{D_3^{(i)}}(0^+) - \overline{D_3^{(i)}}(0^-) = \varepsilon_o k - \overline{D_3^{(i)}}(0^-)$. The shorted condition at the boundary requires $D_3(x_1, 0^+) = 0$ or $\overline{D_3^{(i)\prime}} = \overline{D_3^{(i)}}(0^-)$. To facilitate calculation of the Green's function, the eigenvalue problem in (1.9) and (1.15) is written as

$$(\alpha^2 A_1 - j\alpha A_2 + A_3)\begin{Bmatrix} \overline{u} \\ \overline{\phi} \end{Bmatrix} = 0 \tag{1.29}$$

and

$$\frac{1}{k}\begin{Bmatrix} \overline{T} \\ \overline{D} \end{Bmatrix} = (\alpha A_1 - jA_4)\begin{Bmatrix} \overline{u} \\ \overline{\phi} \end{Bmatrix} \to \alpha A_1\begin{Bmatrix} \overline{u} \\ \overline{\phi} \end{Bmatrix} = \frac{1}{k}\begin{Bmatrix} \overline{T} \\ \overline{D} \end{Bmatrix} + jA_4\begin{Bmatrix} \overline{u} \\ \overline{\phi} \end{Bmatrix} \tag{1.30}$$

Substitution of (1.30) into (1.29) gives

17

$$\alpha\left[\frac{1}{k}\left\{\frac{\overline{T}}{\overline{D}}\right\} + jA_4\left\{\frac{\overline{u}}{\phi}\right\}\right] - j\alpha A_2\left\{\frac{\overline{u}}{\phi}\right\} + A_3\left\{\frac{\overline{u}}{\phi}\right\} = 0 \rightarrow \alpha\frac{1}{k}\left\{\frac{\overline{T}}{\overline{D}}\right\} + j\alpha\left(A_4 - A_2\right)\left\{\frac{\overline{u}}{\phi}\right\} = -A_3\left\{\frac{\overline{u}}{\phi}\right\} \quad (1.31)$$

Combining (1.31) with (1.30) yields the new eigenvalue problem,

$$\alpha\left[\begin{array}{c|c} 1 & j(A_4 - A_2) \\ \hline 0 & A_1 \end{array}\right]\left[\begin{array}{c} T_{13}/k \\ T_{23}/k \\ T_{33}/k \\ D_3/k \\ u_1 \\ u_2 \\ u_3 \\ \phi \end{array}\right] = \left[\begin{array}{c|c} 0 & -A_3 \\ \hline 1 & jA_4 \end{array}\right]\left[\begin{array}{c} T_{13}/k \\ T_{23}/k \\ T_{33}/k \\ D_3/k \\ u_1 \\ u_2 \\ u_3 \\ \phi \end{array}\right] \quad (1.32)$$

At stated by Qiao et. al [23] equation (1.32) is a standard eigenvalue problem of the form $\alpha Bx = Ax$ that yields the eigenvalues and their corresponding eigenvectors together. In contrast, the traditional method determines the eigenvalues $\alpha^{(m)}$ first; then uses them to obtain the four corresponding eigenvectors in a piecewise fashion.

C. Hybrid Method

In this method calculating the Green's function uses a mixture of both methods to eliminate numerical instabilities in the generalized method while obtaining a high degree of precision in the solution. Since the numerical magnitude ranges from 10^{12} to 10^{-12} for the values in (1.32), even the most robust eigenvalue solver has great difficulties. First equation (1.32) is solved for the eight values of $\alpha^{(m)}$ then four are selected for the appropriate propagating mode. Each eigenvalue is substituted into (1.32) yielding,

$$\alpha^{(m)}Bx = Ax \rightarrow \left(\alpha^{(m)}B - A\right)x = 0, \rightarrow Qx = 0, m = 1...4 \quad (1.33)$$

where

$$B = \left[\begin{array}{c|c} 1 & j(A_4 - A_2) \\ \hline 0 & A_1 \end{array}\right] \quad (1.34)$$

$$A = \begin{bmatrix} 0 & -A_3 \\ \hline 1 & jA_4 \end{bmatrix} \qquad (1.35)$$

Each eigenvalue $\alpha^{(m)}$ allows row-reduction of Q to determine the null basis for (1.33), in which are eight element column vectors comprising $\begin{bmatrix} \bar{T} & \bar{D} & \bar{u} & \bar{\phi} \end{bmatrix}$. This approach obtains the precision of the traditional method, while using the general method to solve the entire problem without computing C_m explicitly from the boundary matrix.

1.2.2 Static IDT Capacitance

From equivalent circuit considerations the IDT can be described by a circuit consisting of static capacitance (C_s), radiation conductance (G_a), electric losses (G_l), imaginary part of the admittance (B_a), and a series resistance (R_s). The static capacitance typically dominates the imaginary part of the input admittance and therefore must be precisely calculated. The admittance corresponds to the effect of acoustically induced charges on the transducers due to the piezoelectricity of the substrate material [24]. The most important parameters are the static capacitance (C_s) given that it is the major part of the load seen by the driving circuitry and the radiation conductance (G_a) as it contains information regarding the acousto-electric conversion efficiency. Devices that lack shielding or confinement of the fluid between the IDTs are strongly dependent on electrical properties of the fluid, causing the sensor to detect these properties rather than mechanical interactions during recognition layer-ligand binding. In some cases shielding is not desirable, for example when measuring the conductivity and permittivity of ionic solutions [25-27].

Evaluation of the static capacitance requires solving for the induced charge distribution on the IDTs as a result of an applied voltage. This can be accomplished by using several methods that include the Method of Moments (MoM) [28], Finite Element Methods (FEM), Green's function [29-31], spectral domain representation [32] and even conformal mapping [33] for simpler geometries. By using $C_t = Q/V$, the total static capacitance can be computed from the charge. For IDTs composed of uniform strip widths with a periodicity (p) in Fig. 2,

the total capacitance is computed from $C_t' = (N\text{-}1)WC_t$, where N is the number of electric periods and W is the length of finger overlap.

For periodic structures simplifications can be made to reduce the computational effort. The static capacitance is directly related to the Fourier transform of transducer polarity sequence for both single and split finger periodic IDTs. The following relationship for charge $Q_m'(\eta)$ on the m$^{\text{th}}$ electrode given by [34]:

$$Q_m'(\eta) \square \frac{Q_m(\eta)}{(\varepsilon_0 + \varepsilon_p)WV_o} = 2\int_0^1 \sin(\pi s)\frac{P_{-s}(\cos(n\pi))}{P_{-s}(-\cos(n\pi))}e^{-j2\pi ms}ds \tag{1.36}$$

can also be expressed as [32],

$$Q_s(\eta) = 4(\varepsilon_o + \varepsilon_p)W\int_0^1 \cos^2\left(\pi\frac{t}{2}\right)\left[\sin(\pi t)\frac{P_{-t/2}(\eta)}{P_{-t/2}(-\eta)}\left|\sum_{n=0}^{N-1}\frac{V_n}{V_T}e^{-j2\pi nt}\right|^2\right]dt \tag{1.37}$$

for n split electrodes, where ε_o is the permittivity for vacuum, ε_p is the effective substrate permittivity, W is the transducer width and $P_\nu(\eta)$ is the legendre function of the first kind and order ν for which the symmetry relation $P_{-\nu}(\eta) = P_{\nu-1}(\eta)$ holds. The legendre function $P_\nu(\eta)$ is given by

$$P_\nu(\eta) = \sin\left(\frac{\eta\pi}{2}\right)\frac{\sqrt{2}}{\pi}\int_0^{\eta\pi}\frac{\cos\left[\left(\nu+\frac{1}{2}\right)\theta\right]}{\sqrt{\cos(\theta)-\cos(\eta\pi)}}d\theta \tag{1.38}$$

For the particular case of $\eta = 0.5$, the expression given by (1.36) can be written as

$$Q_m'(\eta = 0.5) = \frac{4}{\pi}\frac{1}{(1-4m^2)} \tag{1.39}$$

For double split IDTs there are now $2n$ electrodes such that (1.38) is found to be [32],

$$Q_s(\eta) = 4(\varepsilon_o + \varepsilon_p)W\int_0^2 \cos^2\left(\pi\frac{t}{2}\right)\left[\sin(\pi\frac{t}{2})\frac{P_{-t/2}(\eta)}{P_{-t/2}(-\eta)}\left|\sum_{n=0}^{N-1}\frac{V_n}{V_T}e^{-j2\pi nt}\right|^2\right]dt \tag{1.40}$$

To address any combination of dielectric layers or media (e.g. waveguides or fluids) on the piezoelectric substrate, it is ideal to use finite element methods (FEM). The approach is

to solve Poisson's equation (1.41) for the geometry shown in Fig. 2 then compute the electric field and electric displacement according to (1.42) and (1.43):

$$-\nabla \cdot \left(\varepsilon \nabla \Phi \right) = 0 \tag{1.41}$$

$$\vec{E} = -\nabla \Phi \tag{1.42}$$

$$\vec{D} = \varepsilon \vec{E} \tag{1.43}$$
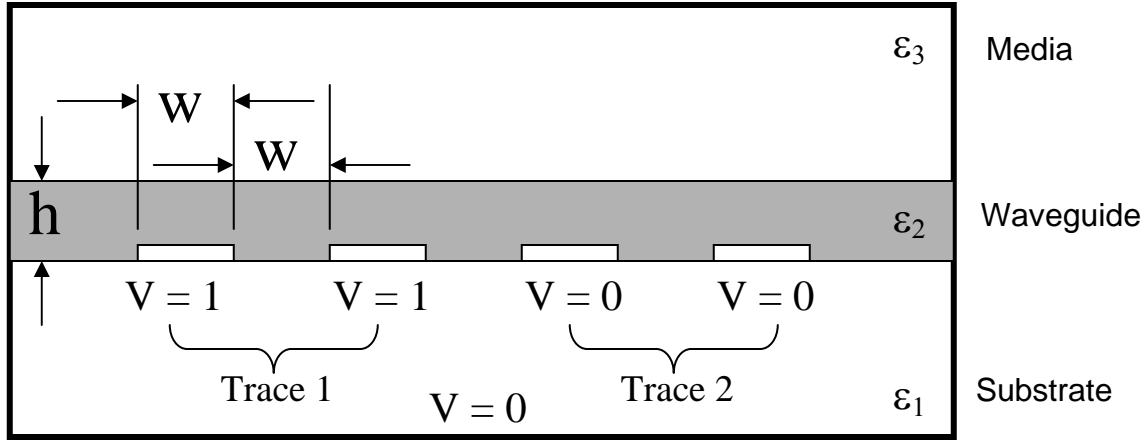
Fig. 2 Depicted is a double split IDT geometry with two alternating electrodes held at $V = 1$ and $V = 0$.

By placing a known voltage on the metalized regions (e.g. $V = 1$, $V=0$), two methods can then be used to extract the capacitance of the IDT's. The total induced charge can be obtained from using:

$$Q = \oiint \vec{D} \cdot d\vec{s} = CV \tag{1.44}$$

The dot product in the integral represents the flux through a two dimensional surface surrounding the structure or simply the line integral. Computational this method is fast, however it is also less accurate since the total flux is highly dependent on the location of the line integral boundary. A more accurate method is to compute the total energy in the electric and displacement fields then equate this to the capacitance expression for stored energy:

$$U = \frac{1}{2} \int \vec{E} \cdot \vec{D} dA = \frac{1}{2} CV^2 \tag{1.45}$$

Since the permittivity of LTO is a 2$^{\text{nd}}$ rank tensor, the permittivity is often approximated by

$$\varepsilon_\infty = \varepsilon_0 + \varepsilon_p = \varepsilon_0 + \left[\varepsilon_{11}^T \varepsilon_{33}^T - \left(\varepsilon_{13}^T \right)^2 \right]^{1/2} \qquad (1.46)$$

However, we must exercise caution when using (1.46) since this form of the effective permittivity is only valid for weakly coupled substrates such as quartz. From exact effective permittivity theory, $\varepsilon(\infty)/\varepsilon_o = 49.7$, where the approximation gives $\varepsilon(\infty)/\varepsilon_o = 42.3$ for 36° YX LTO (Appendix C). The approximation is reasonably valid however for other strongly coupled modes; the effective permittivity must be computed for the general problem.

1.2.3 Love Waves: Lossless Two Layer Case (Non-piezoelectric)

Love Waves are guided waves of horizontal shear polarization (SH), usually propagating within a thin (guiding) layer of material attached to a substrate of higher shear velocity. The waves are dispersive (e.g. frequency or thickness dependent) and dependent on the relative change in the material properties between the layer and the substrate. To begin we consider a plane wave propagating in isotropic layers where piezoelectric effects and material losses have been neglected. The substrate layer is modeled as a half space such that displacement must decay with increasing depth to have a bounded solution.

In Fig. 3, the substrate has a density ρ_1, and Lamé constants μ_1 and λ_1 where the guiding layer has a density ρ_2, Lamé constants μ_2 and λ_2 and thickness h. The existence of a wave is dependent on the boundary conditions and the specification that the propagation constants are real values since there are no losses in the layers.
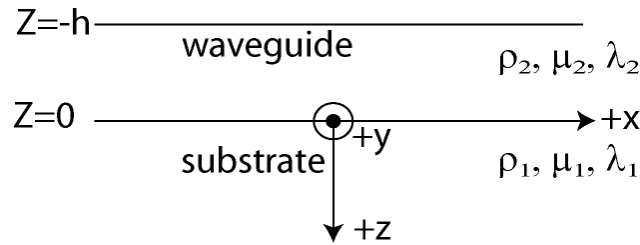

Fig. 3 Love wave configuration on a half-space

The propagation constants ν_1 and ν_2 are defined as:

$$\nu_1 = k_{\beta_1}^2 - k^2 \qquad (1.47)$$

22

$$V_2 = k_{\beta_2}^2 - k^2 \qquad (1.48)$$

where, k is the wavenumber of the propagating Love Wave, k_{β_1} is the wavenumber in the substrate, and k_{β_2} is the wavenumber in the waveguide. The wavenumber for the substrate and the waveguide are determined by their material properties at the operating frequency. The velocity in the substrate and the waveguide are specified by $\beta_1 = \sqrt{\mu_1 / \rho_1}$ and $\beta_2 = \sqrt{\mu_2 / \rho_2}$, respectively. In terms of the angular frequency (ω), material density (ρ) and shear modulus (μ), the wavenumbers can be expressed as

$$k_{\beta_1}^2 = \frac{\omega^2}{\beta_1^2} = \frac{\omega^2 \rho_1}{\mu_1} \qquad (1.49)$$

$$k_{\beta_2}^2 = \frac{\omega^2}{\beta_2^2} = \frac{\omega^2 \rho_2}{\mu_2} \qquad (1.50)$$

where, ρ_1 is the density in the substrate, ρ_2 is the density in the waveguide, μ_1 is the substrate modulus, and μ_2 is the waveguide modulus. For a propagating SH plane wave we have the following displacements for the substrate (u_1) and the waveguide (u_2) as and as:

$$u_1 = A e^{-V_1 z} e^{i(\omega t - kx)} \qquad (1.51)$$

$$u_2 = \left(B e^{-V_2 z} + C e^{V_2 z} \right) e^{i(\omega t - kx)} \qquad (1.52)$$

where, t is time and x is the position along the x-axis. The constants A, B, and C are unknown amplitude constants specified by application of the boundary conditions. The boundary conditions require that the wave displacement is continuous across the interface, the interfacial stresses (T_{ij}) match at the interface and that traction for u_2 vanishes at z = -h for a free surface. This is stated as:

$$\mu_1 \frac{\partial u_1}{\partial z} = \mu_2 \frac{\partial u_2}{\partial z}\bigg|_{z=0} \qquad (1.53)$$

$$\mu_2 \frac{\partial u_2}{\partial z} = 0\bigg|_{z=-h} \qquad (1.54)$$

$$u_1 = u_2\big|_{z=0} \qquad (1.55)$$

By applying the boundary conditions we arrive at the following equations:

$$-v_1\mu_1 A + v_2\mu_2 B - v_2\mu_2 C = 0 \tag{1.56}$$

$$-Be^{v_2 h} + Ce^{-v_2 h} = 0 \tag{1.57}$$

$$A - B - C = 0 \tag{1.58}$$

The non-trivial solution is given by setting the determinant of (1.59) equal to zero,

$$\begin{vmatrix} -v_1\mu_1 & v_2\mu_2 & -v_2\mu_2 \\ 0 & -e^{v_2 d} & e^{-v_2 d} \\ 1 & -1 & -1 \end{vmatrix} = 0 \tag{1.59}$$

After some simplification we have,

$$\frac{e^{v_2 h} - e^{-v_2 h}}{e^{v_2 h} + e^{-v_2 h}} = -\frac{\mu_1 v_1}{\mu_2 v_2} \tag{1.60}$$

We recognize that the l.h.s. of (1.60) can be written as,

$$i\tan(v_2 h) = -\frac{\mu_1 v_1}{\mu_2 v_2} \tag{1.61}$$

In order to obtain real solutions for the acoustic velocity (v_2), v_1 from (1.47) must be made imaginary, which requires that the velocity in the waveguide is less than the substrate e.g. $\beta_2 < \beta_1$. This requires that,

$$iv_1 = i\sqrt{\frac{\omega^2}{\beta_1^2} - k^2} = \sqrt{k^2 - \frac{\omega^2}{\beta_1^2}} \tag{1.62}$$

Inserting this into (1.63) gives the dispersion relationship for Love Wave propagation in the waveguide layer,

$$\tan\left[h\sqrt{\frac{\omega^2}{\beta_2^2} - k^2}\right] = \frac{\mu_1}{\mu_2}\frac{\sqrt{k^2 - \frac{\omega}{\beta_1^2}}}{\sqrt{\frac{\omega}{\beta_2^2} - k^2}} \tag{1.64}$$

24

$$\tan\left[2\pi\frac{h}{\lambda}\sqrt{\frac{v_p^2}{\beta_2^2}-1}\right]=\frac{\mu_1}{\mu_2}\frac{\sqrt{1-\frac{v_p^2}{\beta_1^2}}}{\sqrt{\frac{v_p^2}{\beta_2^2}-1}} \qquad (1.65)$$

The dispersion relationship (1.64) is a transcendental equation and is real valued when $\beta_2 < v_p < \beta_1$, the range of apparent velocities where we have real plane waves in the top layer and evanescent waves in the lower half-space. Expression (1.65) shows the explicit dependence of v_p and h/λ, which is a convenient form for the lossless case. If we rewrite the l.h.s as,

$$\tan\left[h\sqrt{\frac{\omega^2}{\beta_2^2}-k^2}\right]=\tan\left[hk\sqrt{\frac{v_p^2}{\beta_2^2}-1}\right]=\tan\left[2\pi\frac{h}{\lambda}\sqrt{\frac{v_p^2}{\beta_2^2}-1}\right]=\tan(\varsigma\frac{h}{\lambda}) \qquad (1.66)$$

where $\varsigma = 2\pi\sqrt{\frac{v_p}{\beta_2^2}-1}$ then the phase velocity is defined as $v_p = \omega/k$.

The l.h.s will have zeroes at $\varsigma = n\pi\lambda/h$, where n is an integer. The r.h.s of (1.64) decreases monotonically with velocities from infinity at $v_p = \beta_2$ to zero at $v_p = \beta_1$. For a given h/λ, the solution is the smallest value of v_p is called the fundamental mode. In fact there exists and infinite number of Love Wave modes that satisfy (1.64).

Now we turn to solving for the displacements in the waveguide and substrate. Using (1.56), (1.57), and (1.58) we now must now solve for A, B, and C using the boundary conditions. This is accomplished by recognizing that $B = C$ for the existence of a sinusoidal propagating Love wave in the waveguide layer, allowing one to rewrite u_2 as:

$$u_2 = \left(Be^{-v_2 z}+Be^{v_2 z}\right)e^{i(\omega t-kx)}=2B\cos(v_2 z)e^{i(\omega t-kx)} \qquad (1.67)$$

The displacement in the substrate (1.51) and the waveguide (1.52) must be equal at $z = 0$. We find from this condition that $B = A/2$ giving u_1 and u_2 as

$$u_1 = Ae^{-v_1 z}e^{i(\omega t-kx)} \qquad (1.68)$$

$$u_2 = A\cos(v_2 z)e^{i(\omega t - kx)} \tag{1.69}$$

This result could have been solved immediately from (1.59) by computing the eigenvalue (v_p) and corresponding eigenvector. In this case, the eigenvalue must appear explicitly in (1.59) for the computation. The amplitude A depends on the density of the power transported down the guiding layer.

1.2.4 Mass Sensitivity Analysis

Gravimetric sensors are usually configured in two types of instrumentation: oscillation frequency measurement and phase velocity measurements. For SAW delay lines the sensitivity is defined as a measure of the intrinsic properties of the device as [35]

$$S_m = \frac{1}{V_0} \lim_{\Delta m \to 0} \frac{\Delta V}{\Delta m} \tag{1.70}$$

where V_0 and V are the unperturbed and perturbed phase velocities on the SAW device with $\Delta V = V - V_0$. The perturbation is an infinitesimal thin mass layer $\Delta m = \rho_3 \varepsilon$, where ρ_3 is the density and ε is the thickness of the mass loading layer as shown in Fig. 4. In some cases a delay line can be used in a feedback amplifier such that the frequency is measured at constant phase, giving $\Delta f / f_0 \approx \Delta V / V_0$. There are two kinds of acoustic devices used to construct gravimetric sensors: resonators and delay lines. Acoustic resonators are most often used to form an electrical oscillator; an acoustic delay line sensor can be used in an oscillator circuit or its wave propagation characteristics can be measured directly. Love mode devices are most often configured as acoustic delay lines. The perturbation of the phase velocity in waveguides and of resonance frequency of resonators can be quoted directly to derive the sensitivity formulas of the following two kinds of sensors: 1) oscillator configured by acoustic resonator and 2) phase velocity measurement for acoustic delay lines.
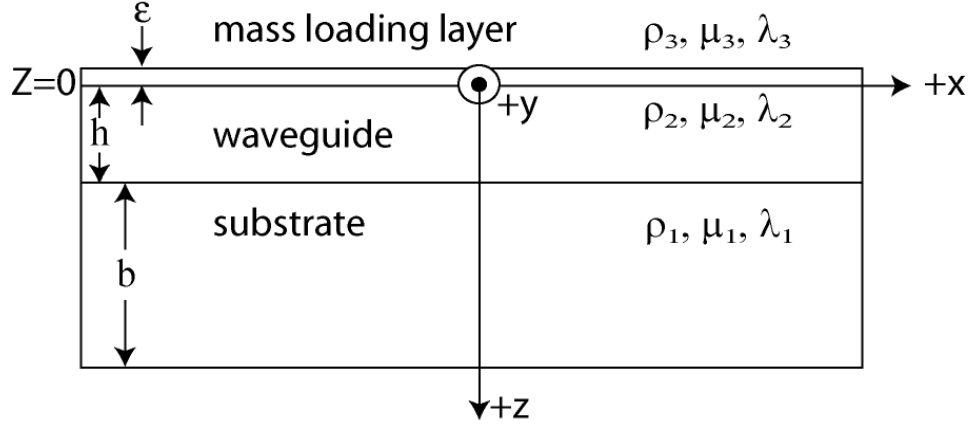
Fig. 4 Configuration and coordinates of the composite and mass loading layer. For the mass layer, μ' and λ' are the Lamé constants of the film. For the substrate and waveguide, μ_1 and μ_2 are the modulii.

In Fig. 4 the composite structure is shown with a finite substrate, which resembles physical devices and also extends the analysis to include perturbation at both faces of the composite structure.

Using (1.116) an analytic expression for the sensitivity can be calculated for both RSAW and SH-SAW propagating modes by computing the shift in velocity ($\Delta V/V$) due to the addition of a thin mass layer Δm on the waveguide. In the substrate and waveguide the displacements are taken as,

$$u_1 = A\cos(v_2 h)e^{-v_1(z-h)}e^{i(\omega t - kx)} \tag{1.71}$$

$$u_2 = A\cos\left(v_2 z\right)e^{i(\omega t - kx)} \tag{1.72}$$

These expressions must account for the finite nature of the substrate for proper evaluation of the acoustic power flow down the waveguide. For the SH mode (1.116) (Appendix C) reduces to

$$\frac{\Delta V}{V} = \frac{-V\rho_3 \varepsilon}{4P_a}\left[\left(1 - \frac{\left(\mu_3/\rho_3\right)}{V_p^{\,2}}\right)\left|\dot{u}_y\right|^2\right] \tag{1.73}$$

Substituting for Δm_s (1.73) becomes,

$$\frac{\Delta V}{\Delta m_s} = \frac{-V_p^{\,2}}{4P_a}\left[\left(1 - \frac{\left(\mu_3/\rho_3\right)}{V_p^{\,2}}\right)\left|\dot{u}_y\right|^2\right]_{y=0} \tag{1.74}$$

27

This expression is evaluated in the substrate and waveguide regions shown in Fig. 4. The mass sensitivity analysis requires that the phase velocity (V_p) in calculated using the dispersion problem.

Taking $\partial u / \partial t$ of u_1 (substrate) and u_2 (waveguide) and squaring yields

$$\left| \dot{u}_1 \right|^2 = A\omega^2 \cos^2 \left(v_2 h \right) e^{-2v_1(z-h)} \tag{1.75}$$

$$\left| \dot{u}_2 \right|^2 = A\omega^2 \cos^2 \left(v_2 z \right) \tag{1.76}$$

where the propagation constants v_1 and v_2 are

$$v_1 = k \left(1 - \frac{v^2}{v_1^2} \right)^{1/2} \tag{1.77}$$

$$v_2 = k \left(\frac{v^2}{v_1^2} - 1 \right)^{1/2} \tag{1.78}$$

The acoustic power flow P_a is given as

$$P_a = V_g \left[\int_0^h U^s{}_{av} dy + \int_h^{b+h} U^w{}_{av} dy \right] = V_g \left[\frac{\rho_2}{2} \int_0^h A\omega^2 \cos^2 \left(v_2 y \right) dy \right] + \lim_{b \to \infty} \left[V_g \left[\frac{\rho_1}{2} \int_h^{b+h} A\omega^2 \cos^2 \left(v_2 h \right) e^{-2v_1(y-h)} dy \right] \right] \tag{1.79}$$

where the is area energy density given as

$$U^{(i)}{}_{av} = \frac{\rho}{2} \sum_j \left| \dot{u}_j \left(y \right) \right|^2 \tag{1.80}$$

P_a reduces to

$$P_a = \frac{\rho_2 V_g A\omega^2 h}{4} \left[1 + \frac{\sin \left(v_2 h \right) \cos \left(v_2 h \right)}{v_2 h} + \frac{\rho_1 \cos^2 \left(v_2 h \right)}{\rho_2 v_1 h} \right] \tag{1.81}$$

28

and inserting (1.75), (1.76), and (1.81) into (1.74) gives the mass sensitivity for the SH mode as

$$S_m^V = -\frac{V_p}{V_g} \frac{1 - \frac{(\mu_3/\rho_3)}{V_p^{\,2}}}{\rho_2 h \left[1 + \frac{\sin(v_2 h)\cos(v_2 h)}{v_2 h} + \frac{\rho_1 \cos^2(v_2 h)}{\rho_2 v_1 h} \right]} \tag{1.82}$$

where the acoustic velocity in the bound mass layer is given as $\beta_3 = \sqrt{\mu_3/\rho_3}$. Eq (1.82) shows that the mass sensitivity is also dependent on the acoustic properties of the bound mass layer. When $\beta_3 \sim V_p$, the S_m^V is dramatically reduced. In the case where the properties of the bound mass layer are ignored, the term $\beta_3^2/V_p^{\,2} \to 0$ gives the maximum device sensitivity.

1.2.5 Love Waves: Lossless Three Layer Case (Non-piezoelectric)

In Fig. 5, the substrate has a density ρ_1, and Lamé constants μ_1 and λ_1 where the guiding layer has a density ρ_2, Lamé constants μ_2 and λ_2 and thickness h. The mass layer has an arbitrary thickness of $h = h_2 - h_1$. For this three layer model, again there are no acoustic losses in the layers.
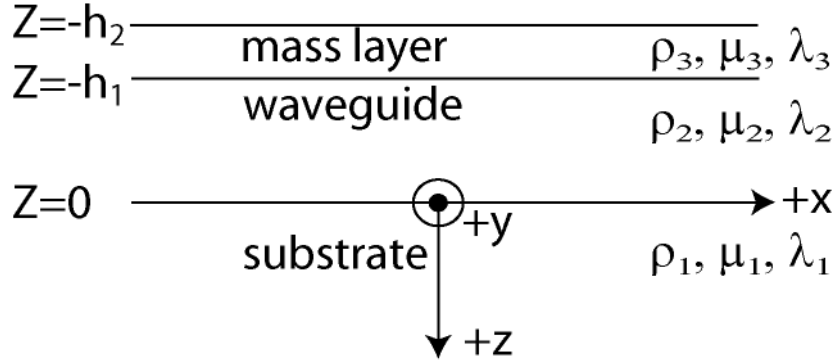

Fig. 5 Configuration and coordinates of the three layer composite with a thick mass layer for the exact isotropic (non-perturbation) analysis.

To derive the dispersion relationship for Fig. 5 we use the following displacement fields for each layer,

$$u_1 = Ae^{-v_1 z} e^{i(\omega t - kx)}$$

$$u_2 = \left(B\cos\left(v_2 z\right) + C\sin\left(v_2 z\right)\right) e^{i(\omega t - kx)} \qquad (1.83)$$

$$u_3 = \left(D\cos\left(v_3 z\right) + E\sin\left(v_3 z\right)\right) e^{i(\omega t - kx)}$$

with the following boundary conditions for continuity of displacements and velocity terms,

$$\mu_3 \frac{\partial u_3}{\partial z} = \mu_2 \frac{\partial u_2}{\partial z}\bigg|_{z=-h_1}$$

$$\mu_2 \frac{\partial u_2}{\partial z} = \mu_1 \frac{\partial u_1}{\partial z}\bigg|_{z=0}$$

$$\mu_3 \frac{\partial u_3}{\partial z} = 0\bigg|_{z=-h_2} \qquad (1.84)$$

$$u_1 = u_2\big|_{z=0}$$

$$u_2 = u_3\big|_{z=-h_1}$$

For a non-trivial solution the determinant of the system of equations resulting from inserting (1.83) into (1.84) must be zero which gives,

$$\tan\left(v_2 h_1\right) = \frac{\cos\left(v_3 h_2 - v_3 h_1\right)\mu_1 v_1 v_2 \mu_2 + \sin\left(v_3 h_1 - v_3 h_2\right) v_2 \mu_2 v_3 \mu_3}{\cos\left(v_3 h_2 - v_3 h_1\right) v_2^2 \mu_2^2 - \sin\left(v_3 h_1 - v_3 h_2\right)\mu_1 v_1 v_3 \mu_3}$$

$$v_1 = \sqrt{k^2 - \frac{\omega^2 \rho_1}{\mu_1}}$$

$$v_2 = \sqrt{\frac{\omega^2 \rho_2}{\mu_2} - k^2} \qquad (1.85)$$

$$v_3 = \sqrt{k^2 - \frac{\omega^2 \rho_3}{\mu_3}}$$

$$\omega = 2\pi f$$

where υ_1, υ_2, υ_3 are the propagation constants for the respective layers. The dispersion relationship is solved using numerical methods that compute k for given materials constants and specified thickness of the waveguide and mass layers.

1.3 MATERIALS AND METHODS

1.3.1 Fabrication

Fabrication of the 325MHz SH-SAW sensor array is based on standard microelectronic processes. The substrate of the sensor is 100 ± 0.2 mm x 0.5 ± 0.02 mm a lithium tantalate wafer which cut is 36° from the Y-axis with the acoustic propagation path in the X-axis direction. The wafer is front side polished to less than 0.6nm with the back side roughness ground to a Ra of 250-500 nm. The reference flat is located along the X-axis with a width of 32mm. The wafers were obtained from Sawyer (1601 Airport Road, Conroe, TX, 77301). The process for fabricating the sensors includes the following steps: 1, wafer preparation; 2, patterning electrical conductors; 3, waveguide deposition and patterning; and 4, dicing and cleaning.

Step 1 – Wafer Preparation

The wafers are specified to be cleaned from the foundry. If the wafer is to be reworked then it is cleaned using a combination of solvent (acetone/isopropanol/methanol) rinses and acid (1% HF) bath soak for enough time to remove the metals and/or oxides. In addition, difficult to remove organic materials such as hard-baked photoresists can be removed by using an oxygen plasma strip (PVA Tepla barrel asher in the MESA uFAB) for approximately 15-30 minutes, but may require up to 90 minutes at 600 watts.

The wafers were treated for 5 minutes in a 1:1:5 $NH_4OH : H_2O_2 : H_2O$ solution at room temperature. This solution was found to clean the wafers and prepare the surface for better adhesion to the photoresist chemical in the first step. The wafer is then rinsed in a cascaded DI water bath until the resistivity exceeds 14MΩ-cm. Filtered house nitrogen at approximately 60 psi is used to blow dry the wafer.

Step 2 – Electrical Conductors

The next step is to pattern the metal electrodes on the polished side of the substrate that will form the interdigitated transducer electrodes, grounded delay line, and buss lines. These structures are accomplished in a single set of steps with the metal being 200 angstroms of titanium for adhesion followed by 5000 angstroms of aluminum.

The backside (rough-side) of the wafer is first spin coated with approximately 3 microns of AZ2020 negative-tone lift-off (AZ2020 nLOF) photoresist. The spinner is Karl-Suss with the lid closed but no Gyrset lid installed, 2000 rpm, 3000 rpm/s, 30 seconds (recipe 2), 5 mL of resist deposited in the center of the wafer. The wafer is baked on a 6-inch silicon wafer (rough-side up, see Fig. 6) placed on a hot plate at 110 °C. The rough-side of the silicon

wafer prevents the lithium tantalate wafer from temporarily bonding electrostatically to the hotplate which increases the likelihood of the wafer breaking as it is heated and expanded. The bake time is 5 minutes after which the wafer is quickly cooled on a metal table.
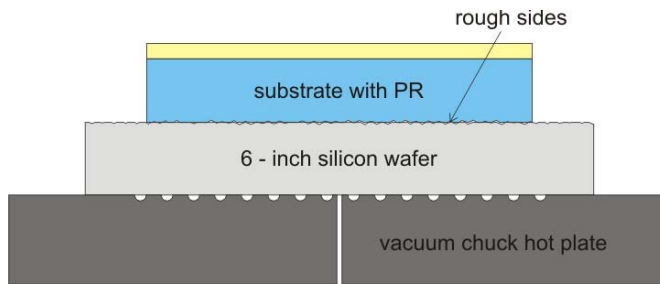

Fig. 6 Schematic of wafer baking technique to avoid breaking wafer.

The wafer is then rinsed in a DI water bath followed by a DI water spray rinse for 1 minute to remove charged particles that are electrostatically attracted to the wafer due to the pyroelectricity of lithium tantalate. The wafer is then dried with a N_2 stream.

The front-side of the wafer is then spin coated with 2.0 microns of AZ2020 nLOF with the Karl-Suss aligner, no Gyrset, lid closed, 3000 rpm, 3000 rpm/s, 30 seconds (recipe 3), 5 mL of resist. The wafer is then baked as before at 110°C for 60 seconds followed by rapid cooling on a room temperature metal table. The wafer is dipped in DI water to discharge the substrate. The photoresist on the back-side of the wafer may partially adhere to the silicon wafer and cause a semi optical opaqueness in these areas which is detrimental to the exposure step. This may be avoided by developing a process for baking the photoresist in an oven and suspending the substrate at the edges. The wafer is dried thoroughly in N_2.

The IDT, buss, and delay line patterns are transferred to the wafer using a chrome on quartz photomask (Photronics, Inc., 15 Secor Road, Brookfield, CT, 06804). The most recent mask used is based on the 325MHz B design revision 3 (325B3). Specifically the Photronics Device# is *SH-SAW 325 B3* and Part# is *Metal*. The exposure is made at i-line wavelength and 27.5 mJ/cm^2 of intensity. The Karl-Suss MA-6 aligner (MESA uFAB MA63 tool) has a 362nm filter installed and is set at 1.1 mW/cm^2 exposure energy for a 25 second exposure. The mode is vacuum contact and the patterns are aligned to the wafer flat for proper wave propagation direction.

The wafer is baked again (with a 6" Si wafer) at 110°C for 90 seconds followed by a rapid cooling and rinse in DI water. The patterns are then developed in a puddle of AZ 300-MIF

(AZ Electronic Materials) at room temperature for 60 seconds. The pattern is visually clear in the large regions after approximately 45-50 seconds. The extra develop time is to ensure the IDT regions are clear and that there is a slight undercut profile. The wafer is immediately rinsed in DI water until the electrical resistivity if greater than 14 MΩ-cm. Visual inspection of proper patterning is accomplished under the microscope.

The wafer is cleaned prior to metal deposition in an oxygen plasma barrel asher for 1 minute at 600 watts. Care should taken when removing the wafer immediately from the asher as it is hot and the thermal stress resulting from the cold room air contact can cause the wafer to break.

Metal is then deposited on the front-side of the wafer in the Temescal (MESA uFAB TEMS5) electron beam evaporator. The base pressure is 1.0×10^{-6} Torr. The titanium deposition rate is 3 angstroms/second. The aluminum deposition rate is 3 angstroms/second for the first 500 angstroms and 10 angstroms/second for the remainder. The thickness is measured on a monitor and tolerances are kept within ±200 angstroms.

The photoresist is lifted-off in an acetone bath for approximately 1-5 hours. Loosely attached unwanted metal flakes are removed in an acetone stream from a squirt bottle. The wafer is then sprayed with acetone from an air-brush (~50 psi) to remove photoresist residue between the IDT fingers. The wafer was then rinsed in DI water, dried and inspected under the microscope for proper lift-off and pattern replication.

Step 3 – Waveguide Deposition and Patterning

The acoustic waveguide is made from a thin film (up to 1.5 microns) of silicon dioxide (SiO_2). The film is first deposited in a plasma enhanced chemical vapor deposition (PECVD) process and then the area over the electrical contact pads is etched away to allow for RF signal stimulation and reception.

The SiO_2 film is deposited in the Oerlikon PECVD (MESA uFAB CVD2) at 150°C. The recipe used is 150_SiO2 and the deposition time is 410 seconds. Before placing the wafer on the heated platen it is ramped to 150-160°C on a 6-inch silicon wafer (rough-side up) on a hotplate and then transferred to the heated platen of CVD2. The 6-inch silicon wafer is held in the center of the platen using alumina rings with point contacts. The wafer is removed and cooled to room temperature. A monitor can be used to measure the thickness on the Nanospec or the thickness and refractive index on the Woolam ellipsometer.

The wafer is kept on the silicon wafer and put into the vacuum oven at 100°C for 18 minutes for deposition of hexamethyldisiloxane (HMDS). The front side of the wafer is then spin coated with ~3 microns of AZ4330 using the Karl-Suss spin coated, recipe 3 (3000 rpm, 3000 rpm/s, 30 seconds, 10 mL of photoresist). The wafer is baked on a 6-inch silicon wafer (rough-side up) on a 90°C hotplate for 90 seconds followed by a DI water dip and N_2 dry.

The photoresist is exposed in Karl Suss aligner (MESA uFAB MA61) through the photomask, Photronics device # *SH-SAW 325 B3*, part # *WAVEGUIDE*. The mask resolution is much less stringent so the mask is chrome on soda-lime glass. The system is operating at a broad UV range centered at the i-line wavelength (20 mW/cm^2). The mask and wafer were aligned and exposed for 40 seconds in vacuum contact mode (hard contact mode is sufficient though). The wafer is then developed in AZ300-MIF for 3 minutes followed by a DI water rinse until the resistivity is greater than 14 MΩ-cm. The wafer is then dried in a N_2 stream.

The SiO_2 is etched and removed in the reactive ion etcher (MESA uFAB RIE2 or RIE3). The system utilizes an endpoint detection system to monitor etch depth. The etch conditions are: temperature = 25°C, chamber pressure = 10mTorr, flow rate of CHF_3 = 45 sccm, flow rate of O_2 = 5 sccm, forward power = 125 watts (reflected power is typically 0.5 watts with a DC bias of 630 volts). The calculated etch time is approximately 1200 seconds for 0.5 microns and is verified by the endpoint detection system. However, the total etch time is 1800 seconds to ensure that all the oxide is removed. The etch rate of the aluminum is negligle. After the etch the photoresist is left on the wafer for the dicing step.

Step 4 – Post Processing

The 44 die on the wafer are diced, cleaned and packaged for before testing. The dicing saw and process is as follows:

1. Wafer Setup
   a. Coat
      i. AZ4330 and soft-bake (2000 rpm, 90°C for 90 sec)
      ii. If the last step of processing was RIE etch to open SiO_2 in bond pad regions, then there is no need to strip the resist and apply more, just use what is already on the wafer.
   b. Mount to center of dicing tape with features oriented up.
2. Dicing Saw Setup

a. Turn on air

b. Mount cutting wheel

    i. Blade: *Resinoid 777-045-010 or 777-053-010*

c. Turn on saw and set parameters

    i. Mode: *10* (round wafer, alignment required after each pass)

    ii. Spindle speed: *15,000 rpm*

    iii. Forward cut speed: *12 mil/sec (0.305 mm/sec)*

    iv. Dimension 1: *4000 mil (101.6 mm)*

    v. Dimension 2: *4000 mil (101.6 mm)*

    vi. Thickness: *2.5 mil (0.064 mm)*

        1. The correct thickness can be determined by setting the height to 2.7 mil and then performing a single cut in a region just outside of the wafer (*height cut*). The thickness should be reduced incrementally between cuts until a visible line is seen in the tape.

        2. It may be beneficial to temporarily increase the forward cutting speed to 100 mil/sec to reduce time.

    vii. Height: *60 mil (1.524 mm)*

    viii. Index 1: *505.286 mil (12.834 mm)*

    ix. Index 2: *402.165 mil (10.215 mm)*

    x. Angle: *96°*

d. Turn on spindle

e. Perform zero blade function

f. Put mounted sample to center of chuck and lock

g. Align wheel to horizontal street

h. Perform thickness adjustment cut if necessary (step 2.c.vi and make sure the forward cut speed is reset back to 12 mil/sec)

i. Perform kerf width cut and adjust markers on monitor to indicate kerf location and width (which should be slightly larger than the streets)

3. Cut sample (see Fig. 7)

a. Align 1st street to monitor markers

b. Perform single cut

c. Make sure Index is selected

d. Move backward and align if necessary

e. Repeat until 7th street is cut

f. Rotate sample CCW 96° (Index rotation) and if necessary realign to streets
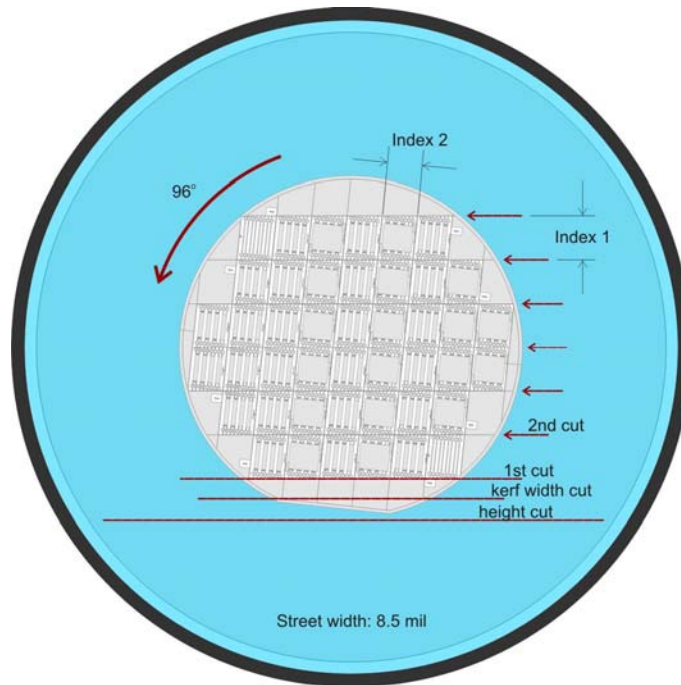
g. Cut streets 1 through 10

Fig. 7 Wafer setup on dicing tape and cut order shown.

After dicing the wafer the die are each individually rinsed with acetone/methanol/isopropanol and then dried in a N_2 stream. It is difficult to completely remove the photoresist using this process and usually some film will remain on the aluminum contact pads. The die are arranged on a 6-inch silicon wafer (rough-side up) and stripped in an O_2 plasma in the PVA barrel asher for 5 minutes, 600 watts. The die are tested for electrical impedance and acoustic characteristics and packaged.

1.3.2 Static IDT Capacitance Measurement via Network Analyzer

The IDT static capacitance in Fig. 2 was determined by measuring S21 using the E8358A vector network analyzer (Agilent Technologies). The static capacitance is related to S21 by

$$C_t = \left| \frac{S21}{2\omega Z_L} \right| \qquad (1.86)$$

For this analysis to be valid we assume,

$$\left| \frac{1}{\omega C_m} \right| >> Z_L = 50\Omega \qquad (1.87)$$

where Z_L is the port impedance of the network analyzer. In general this assumption is valid for low frequency analysis of capacitance, where $\omega/2\pi < 1$ MHz. In this case capacitances up to 10 nF can be easily measured using this method.

1.3.3 Mass Sensitivity Measurement

The mass sensitivity was determined for the Love wave sensors using calibrated fluids with known density and viscosity [36]. Four fluid samples were prepared with known amounts of glycerin and applied to the sensors. Subsequently, the phase shift was measured after each injection and repeated four times. The resulting slope ($\Delta\varphi/\sqrt{\rho\eta}$) was determined by a linear fit procedure and used to calculate mass sensitivity and the detection limit for a given noise level and phase resolution.

1.3.4 Biological Materials and Sensor Preparation

Three IgG antibodies were used to perform multi-analyte detection using the Love wave sensor array. Anti-avidin IgG antibody was obtained from Polysciences Inc. (Warrington, PA). Anti-BSA was purchased from Sigma-Aldrich (St. Louis, MO), and (goat) anti-mouse IgG from Pierce (Rockford, IL). Each antibody was biotinylated using sulfo-LC-biotin (Molecular Biosciences, Boulder, CO). Excess biotinylating agent was removed by centrifugation using YM-50 Millipore Microcon® filters.

The sensors were cleaned in acetone, methanol, and isopropanol, rinsed in distilled water, followed by exposure to UV-ozone for 15 minutes in a UVOCS UV-Ozone cleaner (UVOCS Inc., Montgomeryville, PA). An amine reactive surface was prepared on the SiO_2 waveguides using 1% (3-glycidoxypropyl)trimethoxysilane (3-GPS) in Toluene (Gelest Inc., Morrissville, PA). NeutrAvidin (Pierce, Rockford, IL) was applied to the 3-GPS layer at 0.25 mg/ml for 30 minutes. Each biotinylated antibody was reacted with the NeutrAvidin for 30 minutes using an adsorption cell to confine the antibody types over each

channel. This procedure produced covalently attached IgG antibodies to the SiO_2 waveguides.

1.3.5 Measurements and Data Acquisition

The sensors were measured using an E8358A PNA network analyzer (Agilent, Santa Clara, CA). The data acquisition system was based on the AD8302 (Analog Devices, USA), measuring all four channels simultaneously. Phase data was recorded in real time using an NI USB-6009 National Instruments 14-bit A/D converter at a rate of 1000 samples/second. The data was acquired using both a laptop computer and Personal Digital Assistant (PDA). Fluid injections were performed using a PHD 2000 Harvard syringe pump connected to a six-port two position Rheodyne Nano flow valve (Upchurch Scientific, Oak Harbor, WA). The flow rate was 10 μl / min and fluid cell volume was 4 μl.

1.3.6 Phase Monitoring Circuit

To measure the phase shift of each SH-SAW array, a 4-channel phase monitoring system (Fig. 8) was constructed based on the AD8302 phase/magnitude detection IC (Analog Devices). This IC requires minimal external components and operates using a single supply of 2.7 V–5.5 V. The ac-coupled input signals can range from –60 dBm to 0 dBm in a 50 Ω system, from low frequencies up to 2.7 GHz. The outputs provide an accurate measurement of either gain or loss over a ± 30 dB range scaled to 30 mV/dB, and of phase over a 0°–180° range scaled to 10 mV/degree. This circuit measures the relative phase shift between a reference source and each SH-SAW delay line. The phase tracking circuit provides instantaneous phase data from all four channels. The output ranges from 0 – 1.8V, which corresponds to a phase range of 0°–180° when multiplied by 100 for scaling. The monitoring system was supported using the system in Fig. 9 which provides power, the RF reference source, and computer control. The system in Fig. 10 was battery powered with a run time of ~20 hrs using 2200 mA·hr LiIon battery pack.
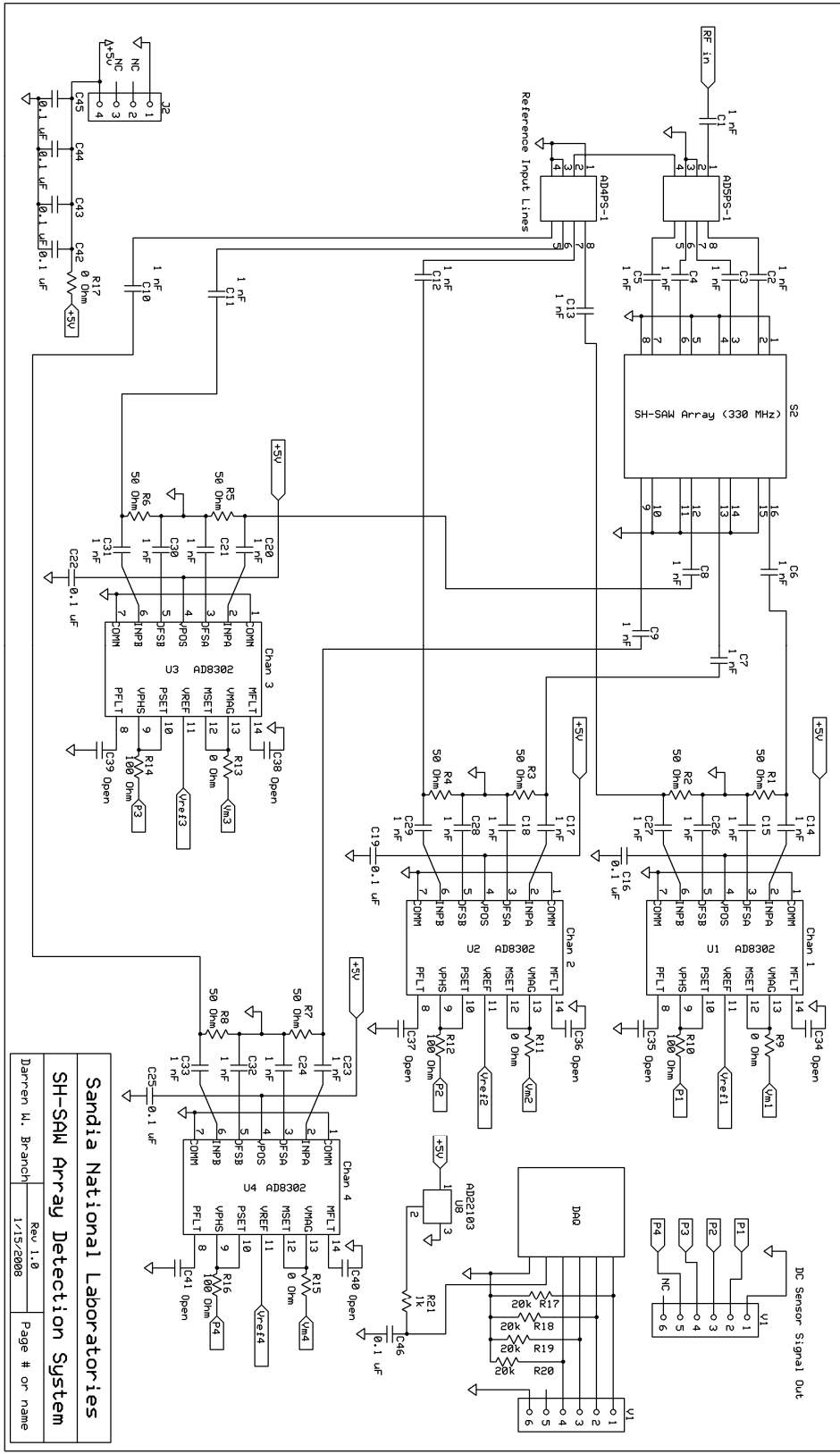
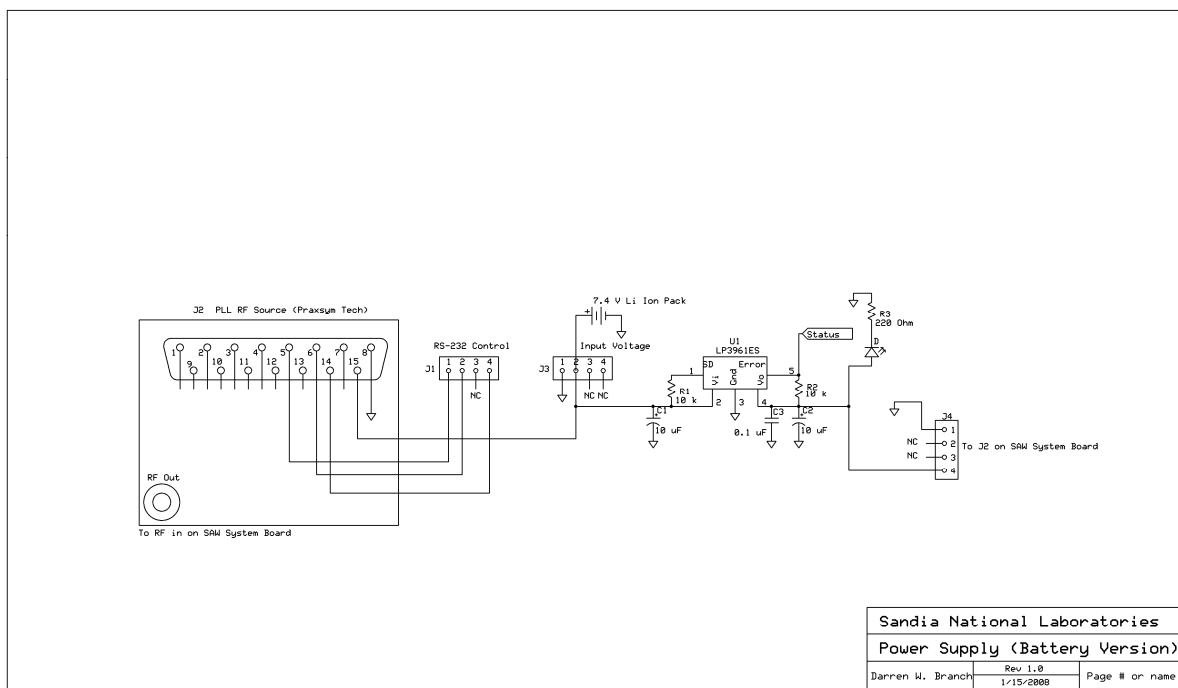**Fig. 8** Phase monitoring system for SH-SAW Array

Fig. 9 Power, RF source, and RS-232 computer control for phase monitoring system.


Fig. 10 SH-SAW Four channel phase detection system connected to a PDA NI CF6004 DAQ card. The sample rate was 1k with a phase resolution of 0.01°
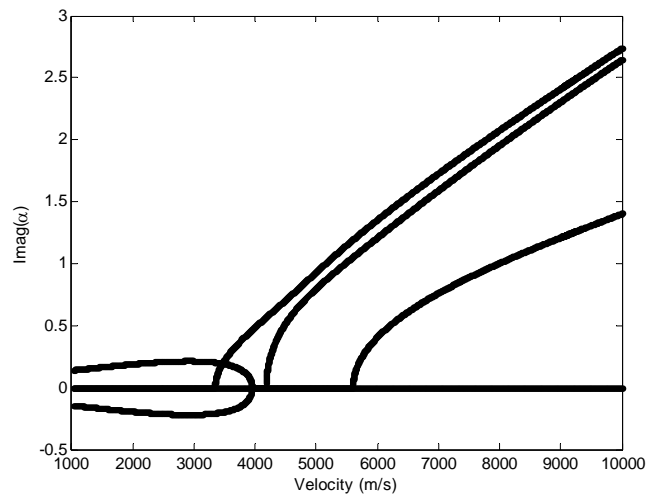
40

1.4 RESULTS AND DISCUSSION

1.4.1 Generalized Green's Function for 36º YX LTO (LSAW)

For 36° YX lithium tantalate the cut-off velocities occur at 3338.1 m/s, 4171.8 m/s, and 5592.4 m/s. Using the eigenvalue selection method the proper values were chosen as shown in Fig. 11. There are three eigenvalues which lead to displacements decaying into solid with
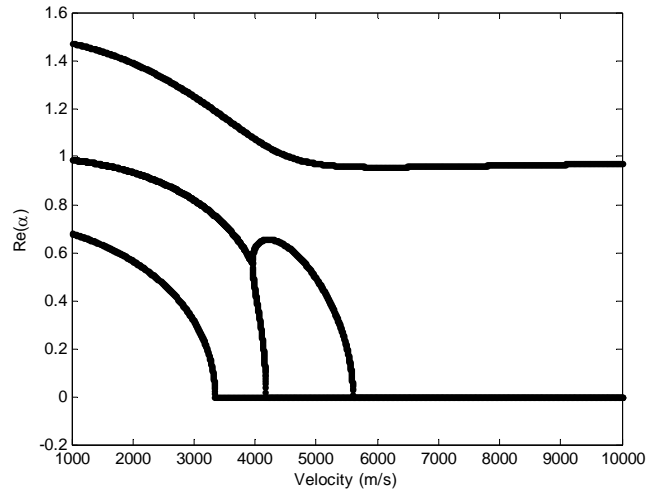
(a)

(b)

Fig. 11 Real and imaginary parts of the allowed values of α as a function of the phase velocity for 36° YX LTO. a) real part of α and b) imaginary part of α.

one bulk wave radiating into the solid. The 4x4 dyadic Green's functions are shown in Fig. 12 and 13.
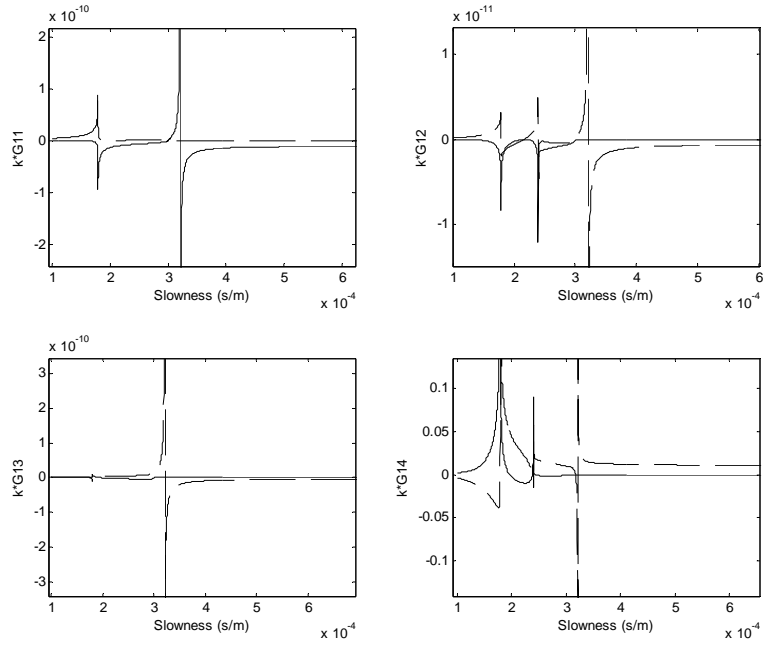
(a)
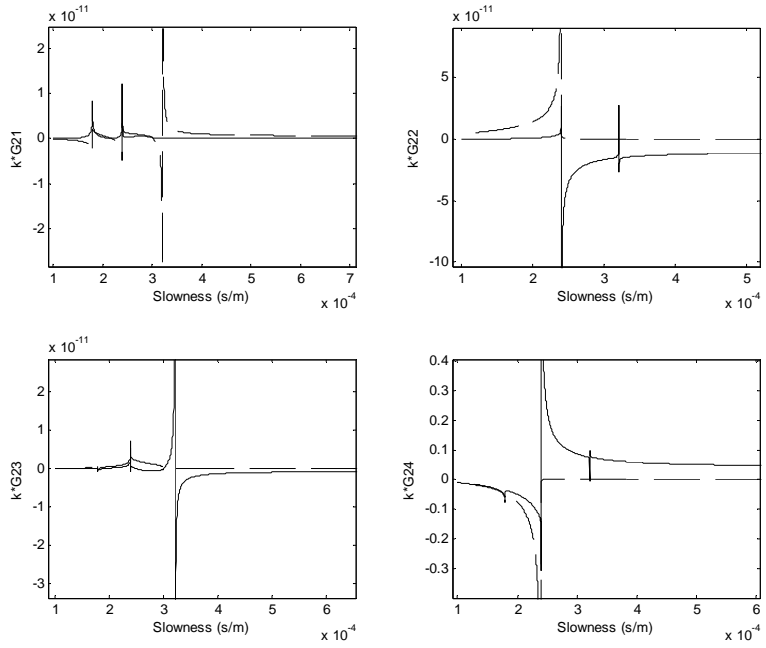
(b)

Fig. 12 Dyadic Green's function for 36° YX LTO showing kG_{11} through kG_{24}.

(a)

(b)

Fig. 13 Dyadic Green's function for 36° YX LTO showing kG$_{31}$ through kG$_{44}$.

1.4.2 Effective Permittivity for 36º YX LTO (LSAW)

For the open condition a pole exists at 4171.73 m/s and for the shorted condition the pole is at 4077.06 m/s (Fig. 14a and b). The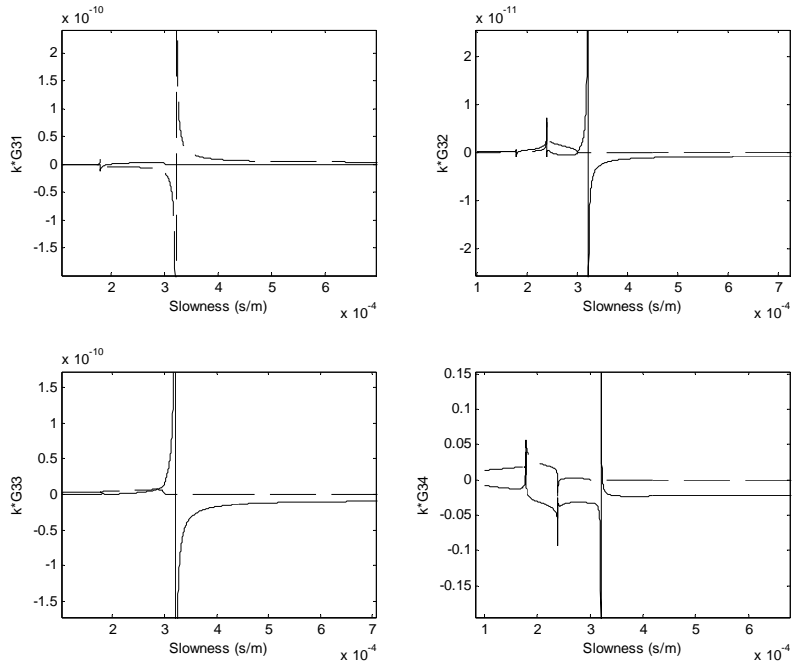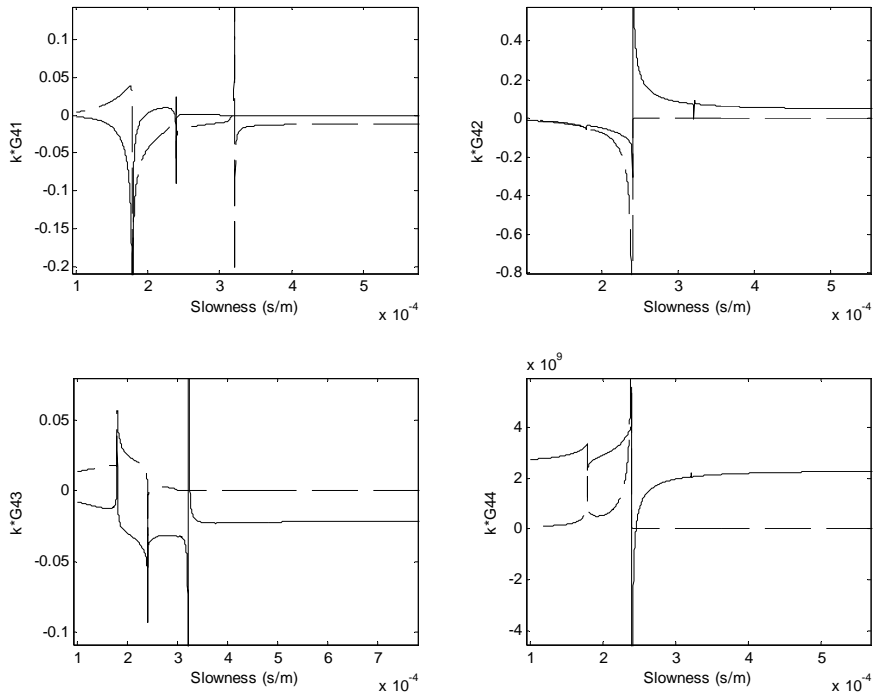 SAW coupling coefficient was computed using $K^2 = 2(V_o-V_s)/V_o$. This gives 4.5% for 36º YX LTO (0º, -54º, 0º). In the shorted condition, the $Im(\varepsilon_s) < 0$ when v < 4171 m/s, which corresponds to partial waves decaying into the substrate. When v > 4171 m/s the $Im(\varepsilon_s) < 0$. This causes bulk wave radiation into the substrate since one of the three the corresponding eigenvalues is complex with a negative imaginary part. In the open condition, the $Im(\varepsilon_o) > 0$ when v > 4171 m/s. Again the eigenvalue α is complex, however with a positive imaginary part. The positive imaginary term leads to surface skimming bulk waves (SSBW) radiating into the substrate as seen by substitution of the different conditions for α into (1.13). The interpretation is that for an open surface, SSBW waves dominate due to the open surface condition, and when the surface is electrically shorted, leaky SAWs (LSAW) dominate.
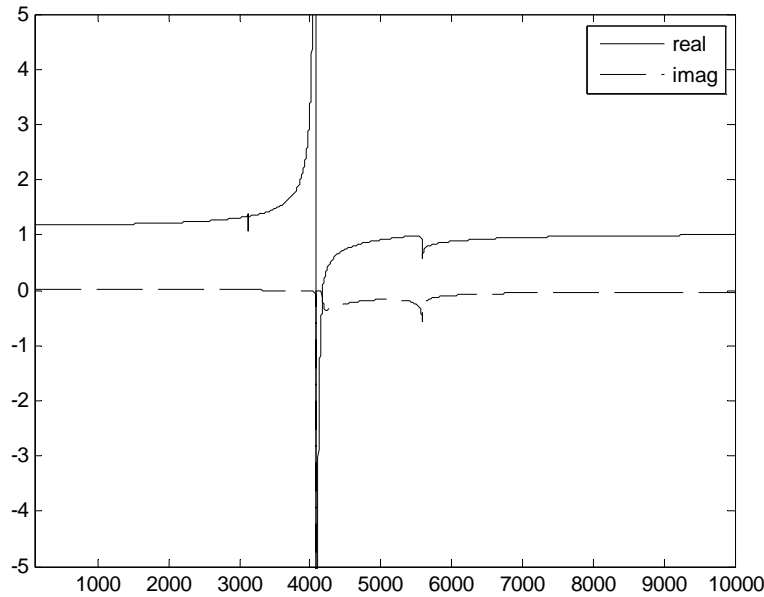

Fig. 14a The normalized effective permittivity for 36º YX LTO (0º, -54º, 0º) for the shorted condition.
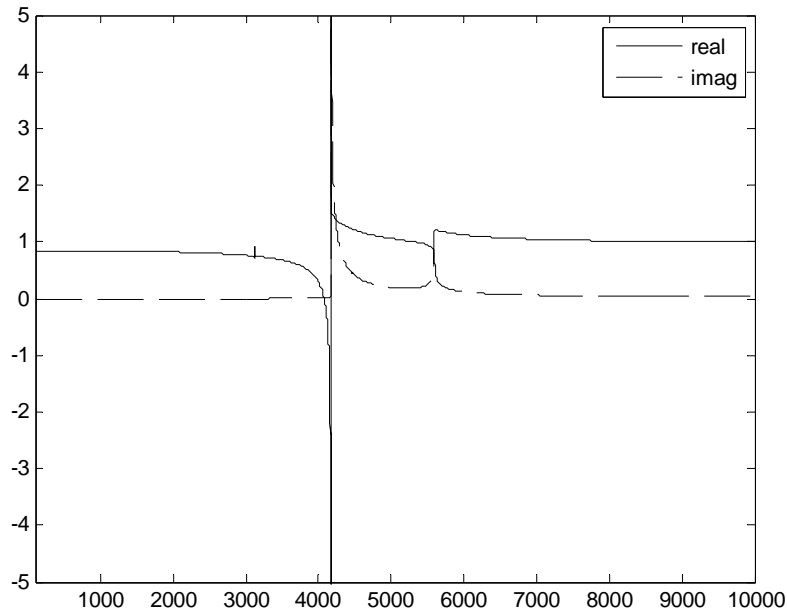
Fig. 14b The normalized effective permittivity for 36º YX LTO (0º, -54º, 0º) for the open condition.

1.4.3 Static IDT Capacitance

Using (1.37) and (1.40), the induced charge can be computed for periodic IDT structures with arbitrary voltages on the electrodes. For example, if the voltage polarity sequence is 0, 1, 1, 1, 0, 0, 1, 1, 0 the normalized static capacitances $(C_t(\eta)/(\varepsilon_o + \varepsilon_p)W)$ for a single and double split IDT are 3.43 pF/m and 4.30 pF/m. Despite the convenience of the expressions described above, they are only applicable to IDTs composed of *uniform strips* in contact with vacuum. This limits the application to IDTs with periodic electrodes and the same strip width to apply superposition principles. In general, the presence of dielectric films on top of the IDTs causes significant deviation in the permittivity such that it will deviate significantly from $\varepsilon_r = 1$, thus requiring a much more detailed analysis. In sensing applications, several dielectric layers may be present on the IDT's in addition to ambient media such as water or saline buffers for biosensor applications.

The static capacitance was calculated for the geometry in Fig. 2 using 2D FEM. The potential has been solved for 36° YX LTO with a polyimide waveguide ($\varepsilon_2 = 3.2$) with water and air as the ambient media (Fig. 15a). As shown in Fig. 15b the external media can cause a large increase in the capacitance when no dielectric insulator in present. In the absence of a dielectric layer, the capacitance varied by over 1000 pF/m from air to water. Even a subtle

45

variation in the ambient media (e.g. buffer, salt concentration) results in substantial variation in the IDT capacitance. To reduce large changes in capacitance, the waveguide thickness must be increased to approximately 8 μm such that the capacitance reaches an asymptotic value. However, application of a suitably thick waveguide layer is often impractical due to physical material limitations and more significantly results in multi-mode acoustic propagation, which reduces the mass sensitivity.
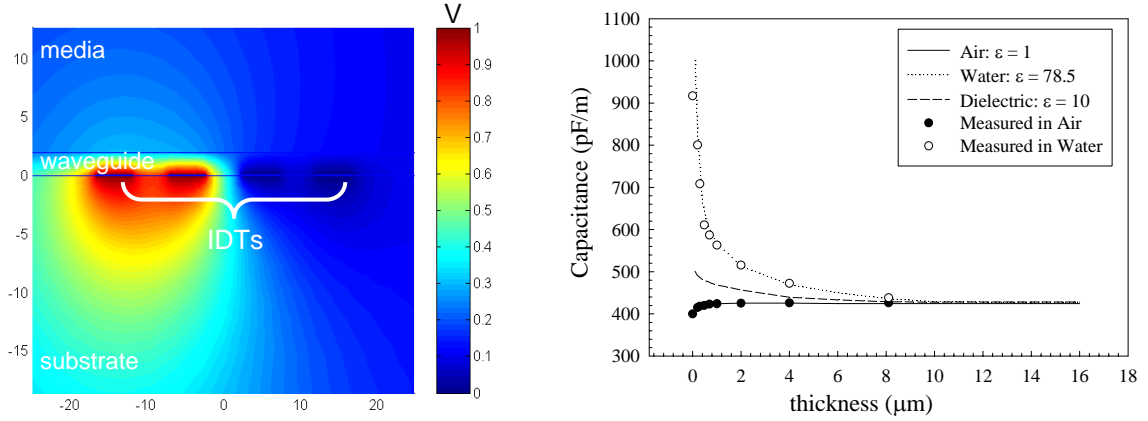
(a)   **(b)**

Fig. 15 Capacitance for double split IDTs on lithium tantalate. **(a)** The substrate, waveguide and water have dielectric permittivity of ε_r = 43.5, 2.9, and 78.5, respectively. **(b)** The computed values for capacitance per length (pF/m) are in good agreement with the experimental measured values.

1.4.4 Dispersion Behavior of Love Waves: Lossless Case (Non-piezoelectric)

By solving (1.64) for the phase velocity (ω/k) as the layer thickness is increased, the dispersive behavior of the layered system can be computed (Fig. 3). An important quantity for the sensitivity calculation is the group velocity given by (Appendix B)

$$v_g = \frac{\partial \omega}{\partial k} = \left[1 - \frac{h/\lambda}{v_p} \frac{d(v_p)}{d\left(h/\lambda\right)} \right]^{-1} \tag{1.88}$$

The group velocity is the velocity of the peak of the wave packet and for lossless propagation it is also the velocity of the energy transported by the wave packet. For guided waves the group velocity is dependent on frequency as opposed to a linear relationship between ω and k for free propagating modes. In the limiting conditions when $h/\lambda \to \infty$, the phase velocity approaches the shear velocity in the waveguide, and when $h/\lambda = 0$, $v_p = \beta s_1$, that is the shear

velocity in the substrate. The calculation assumes isotropic conditions for the substrate and ignores acoustic losses in layers at this point. The highest possible sensitivity is achieved when the shear velocity in the waveguide layer is small compared to the substrate. However, true sensitivity also depends on the acoustic power flow down the waveguide and on the properties of the detected material. We have shown in the sensitivity analysis that the acoustic properties of the attached mass layer strongly alter the device sensitivity.

When the shear velocity in the waveguide is much lower than the shear velocity in the substrate, the slope of the curves is much steeper. There are also more modes for an equivalent waveguide thickness as shown in Fig. 16. This indicates that the waveguide thickness is very critical toward device sensitivity since multimode causes an undesirable distributed of energy amongst the allowed modes. A similar result is obtained for a polyimide waveguide on 36° YX LTO (Fig. 17) where the dispersion curves become much steeper since the shear velocity in polyimide is about 1000 m/s lower. However, our earlier work using polyimide as a waveguide material proved difficult since the material properties vary in fluidic conditions. From a bioconjugation perspective, covalent attachment of receptors to the polyimide waveguide requires significant modification of the surface and degrades adhesion at the piezoelectric-waveguide interface.
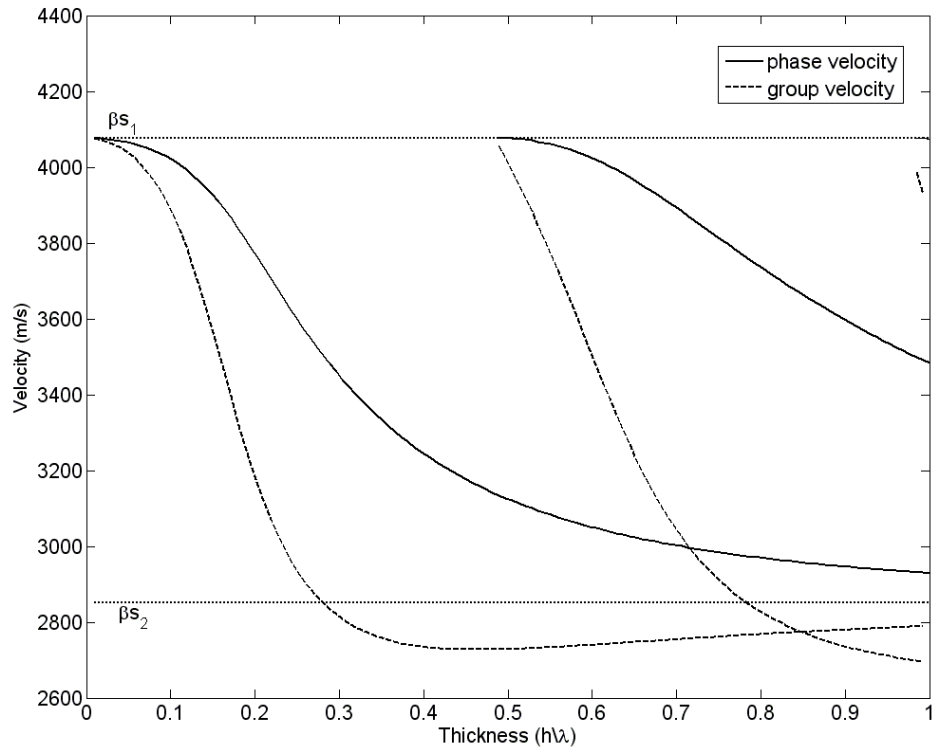
Fig. 16 First two dispersion curves for a SiO$_2$ waveguide on 36° YX LTO (0°,-54°,0°). The dotted lines indicate the shear velocities in the substrate and waveguide.
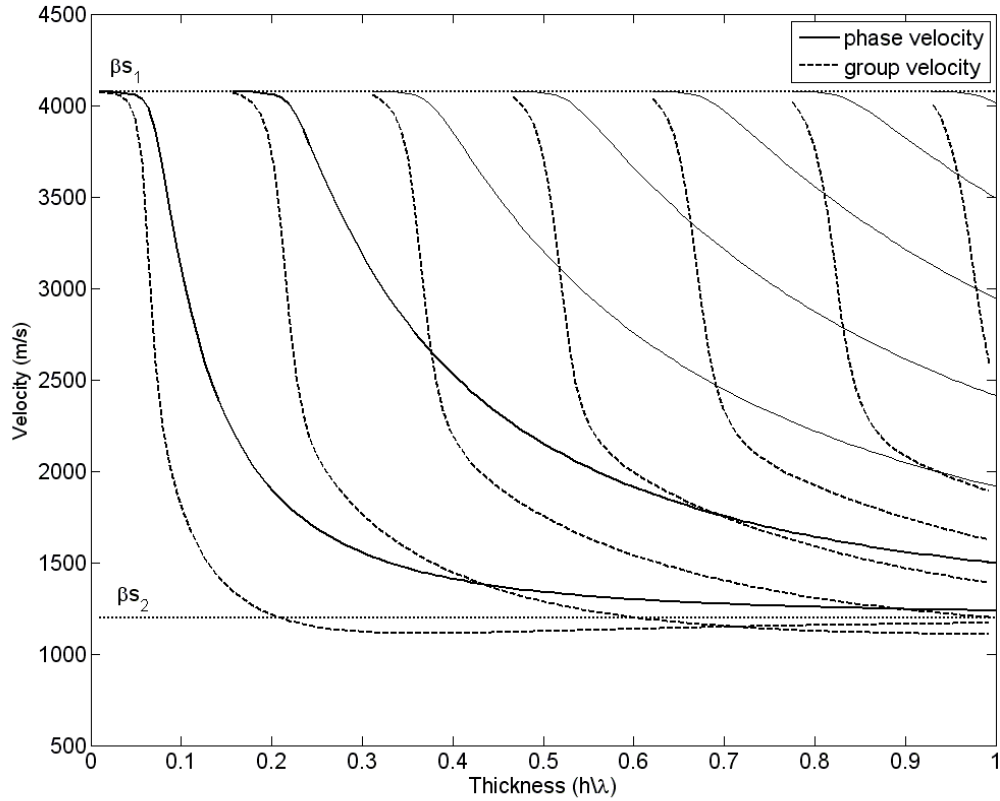
Fig. 17 First seven dispersion curves for a polyimide waveguide on 36° YX LTO (0°,-54°,0°). The dotted lines indicate the shear velocities in the substrate and waveguide.

1.4.5 Comparison of Dispersion Curves for Lossless Isotropic, Piezoelectric, and Measured Group Delay

The dispersion behavior was computed by extending the Green's function method [23] to include an isotropic film and mass layer. From $kG_{44}(s)$, the effective permittivity was computed to find the propagating velocities as the waveguide thickness increased. For comparison, the multilayered problem was analyzed using the lossless isotropic model. In the isotropic case, the substrate phase velocity was taken as $V_s=4040$ m/s since the surface of the LTO is loaded by a 5000 Å aluminum layer. The shear velocity in the waveguide was $V_w=2852$ m/s and mass layer was $V_m=1300$ m/s. The density for each layer was $\rho_s=7450$ kg/m^3, $\rho_w=2200$ kg/m^3, and $\rho_m=1200$ kg/m^3.

The piezoelectric constants for LTO were taken from [37]. In Fig. 18, the dispersion behavior indicates a significant difference between the isotropic and piezoelectric model due

49

to stiffening. Excellent agreement was observed between the measured group and computed group velocity for the SiO_2 waveguide confirming the piezoelectric model.
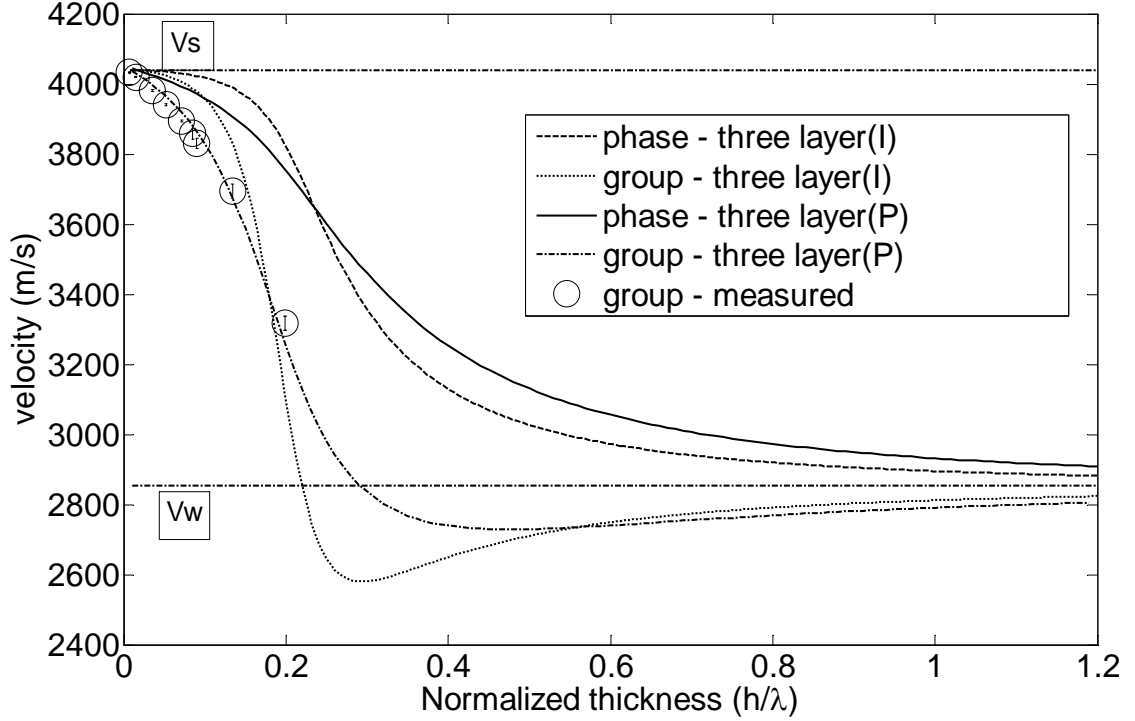
Fig. 18 Dispersion curves for SiO_2 on 36° YX LTO. (I): Isotropic model, (P) Piezoelectric model. The group velocity was measured using time domain analysis. V_s and V_w lines denote the shear velocity in the substrate and waveguide, respectively.

1.4.6 Mass Sensitivity for Lossless Isotropic and Piezoelectric Cases

To determine the sensitivity, the dispersion curves were computed with and without an additional mass layer. The mass sensitivity due to the velocity shift was computed using

$$S_m = \frac{1}{V_0} \lim_{\Delta m \to 0} \frac{\Delta V}{\Delta m} \qquad (1.89)$$

where V is the phase velocity, V_0 is the phase velocity in the absence of the mass layer with mass $m = \rho_m \varepsilon_m$ and ε_m is the thickness of the mass layer. The calculation included the properties of the mass layer ($V_m = 1200$ m/s, $\rho_m = 1300$ kg/m^3). In Fig. 19 the relative error of the optimal thickness (h) was 10 %, whereas the relative error of the maximum sensitivity (S_m) was nearly 70 %. To determine the mass sensitivity for strongly coupled substrates such

as 36° YX LTO, piezoelectric models are clearly required. Since higher operating frequencies require thinner oxide layers the instability and uniformity issues common with thicker oxide layers are reduced.
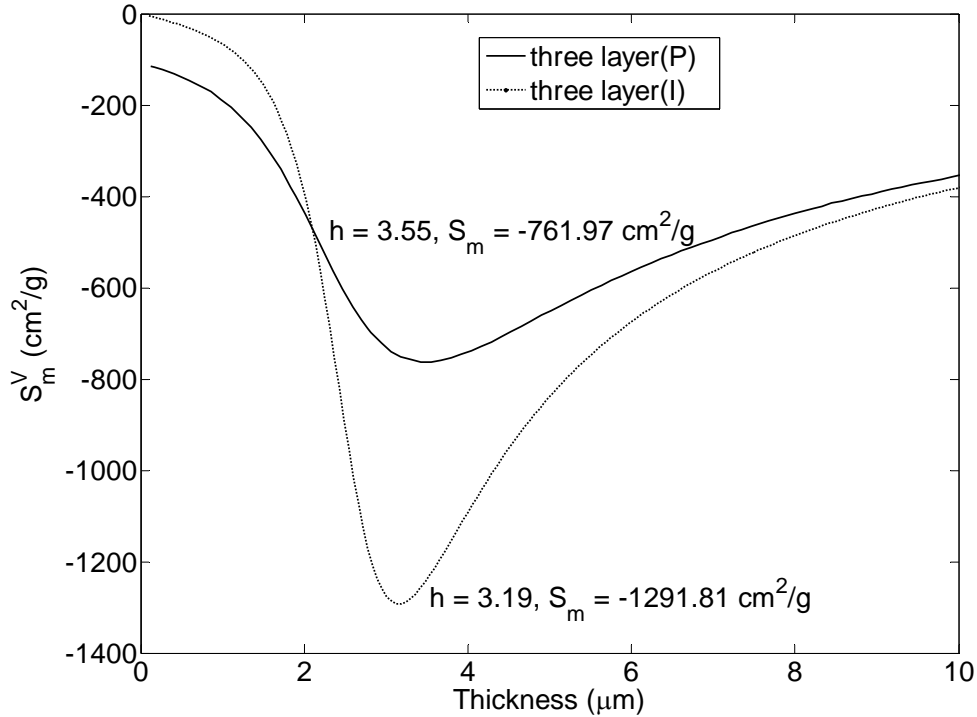
Fig. 19 Sensitivity curves for SiO_2 waveguide on 36° YX LTO using three layer isotropic and piezoeletric models (these were exact models rather than perturbation). (I): Isotropic model, (P) Piezoeletric model. λ=12.4 μm.

1.4.7 Interdigital Transducer Designs and S21 Response

For optimal excitation of SH waves on 36° Y-cut LTO at frequencies in excess of a few hundred MHz, it is necessary to use electrode width controlled single phase unidirectional transducers (EWC-SPUDT). We refer to the standard design by Hartmann [38] which sets the distance from the reflection center to the transduction center as $3\lambda/8$ with the excitation finger as $\lambda/8$ and the reflector as $\lambda/4$ (Fig. 20a and b). Optimization procedures have been developed to tune SPUDT designs for specific substrates that vary from the standard design mentioned above [39]. We evaluated the standard design for use at 330 MHz and created a new design that comprised two reflector types to achieve low insertion loss and high out of band rejection, while minimizing bulk wave excitation near the stop band. Fig. 20 shows the

key design elements of the fabricated transducers. Guard electrodes were included in the design shown in Fig.20c to suppress electric field edge effects.

(a)

Parameters	Scaling
s_1	0.130λ
s_2	0.073λ
s_3	0.324λ
b_1 **(reflector)**	0.237λ
b_2	0.118λ
b_3	0.118λ

(b)

Parameters	Scaling
s_1	0.130λ
s_2	0.073λ
s_3	0.324λ
b_1 **(reflector)**	0.237λ
b_2	0.118λ
b_3	0.118λ

(c)

Parameters	Scaling
s_1	0.125λ
s_2	0.125λ
s_3	0.181λ
s_4	0.194λ
b_1	0.125λ
b_2	0.125λ
b_3	0.125λ
b_4	0.250λ
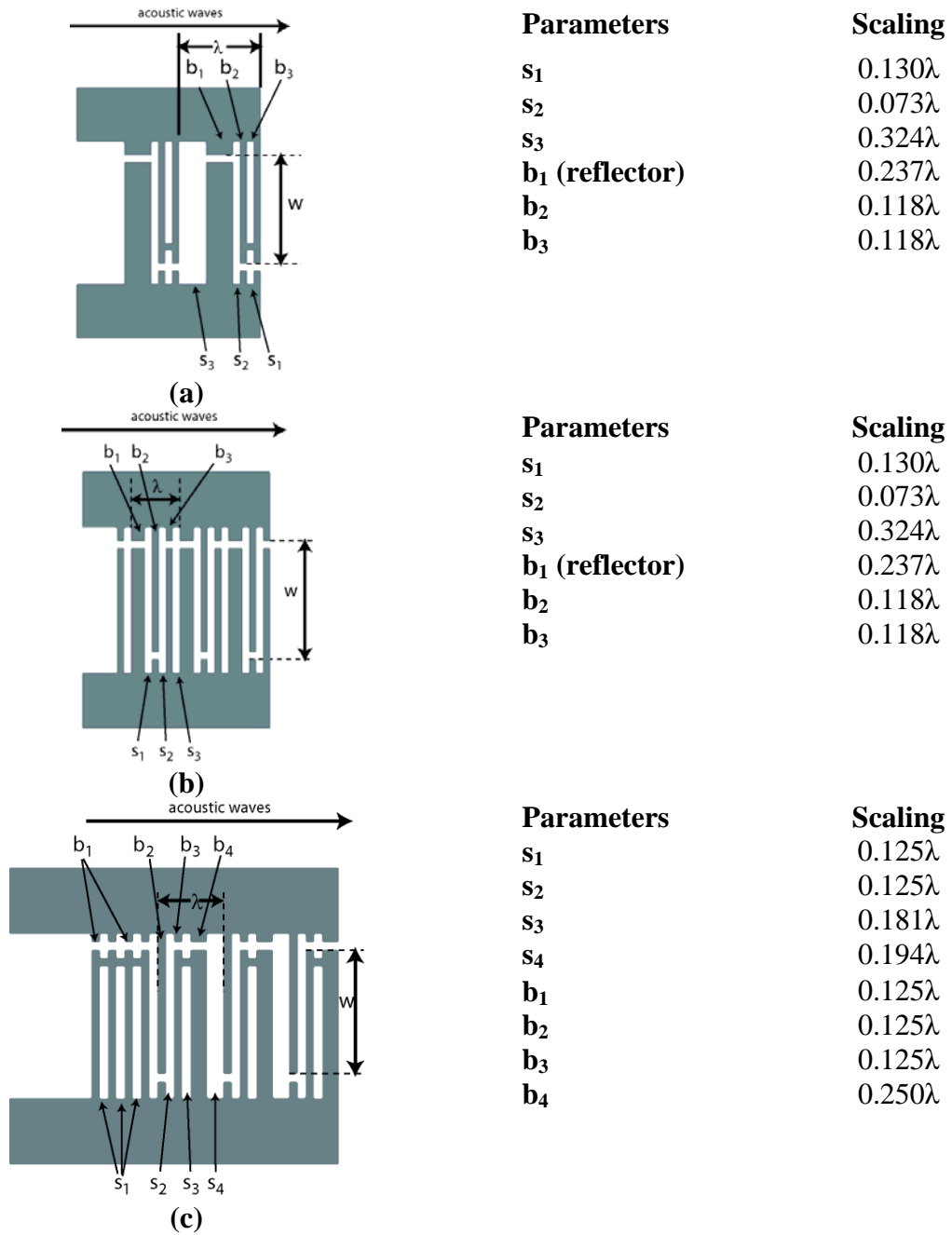
Fig. 20 EWC-SPUDT evaluated in this work a). Double split finger design based where the distance from the reflection centers to the transduction center is $3\lambda/8$ with the excitation finger as $\lambda/8$, b) Alternating design where a single launch center is $3\lambda/8$ from the reflection center, and c) uses an approximate launch-reflector separation of 0.39λ combined with a guard electrode array to reduce electric field edge effects.

The EWC-SPUDT design in Fig. 20a produced a sinc(x) function type response with a phase linearity of 2° P-P (Fig 21a). The drawback of this design was the poor out-of-band rejection at the start and stop bands and the need for high resolution photolithography. The center frequency was limited to 315 MHz since the separation between b_1 and b_2 was ~ 1µm. The addition of the waveguide film only reduced the IL to -9.09 dB.

(a)
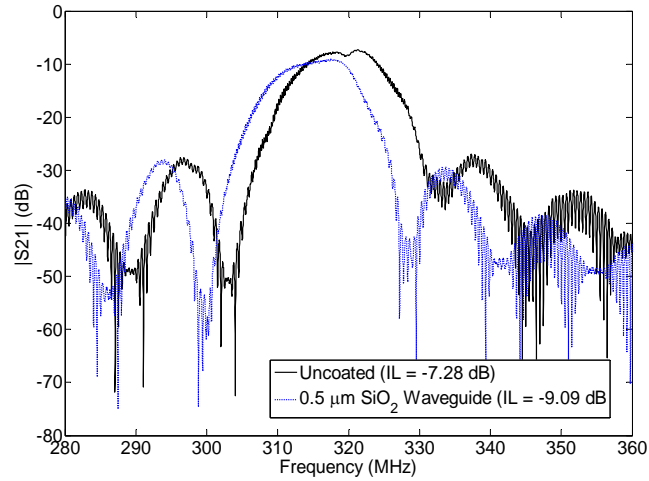
(b)

Fig. 21 Measured S21 response of a 310 MHz Love wave sensor in Fig 20a. a) |S21| (dB) and b) phase (°). Increasing the waveguide thickness increased the phase slope.

The alternate design in Fig. 20b had a less stringent requirement on the photolithographic patterning process since the reflection center from b_1 to b_2 was no longer distributed between two excitation fingers. The S21 response in Fig. 22a has significant improved out-of-band rejection, however with higher phase non-linearity (4.4 ° P-P).

(a)

(b)

Fig. 22 Measured S21 response of a 330 MHz Love wave sensor in Fig 20b. a) |S21| (dB) and b) phase (°). Increasing the waveguide thickness increased the phase slope.

The optimized design (Fig. 20c) shows a highly linear phase response (2.8° P-P) with an insertion loss of −5.43 dB at 330 MHz (Fig. 23). The phase linearity was maintained after the deposition of a 0.5 μm SiO_2 waveguide. The IDT design proved successful in suppressing bulk waves and preferentially exciting the leaky SH mode on 36° YX LTO. The low degree of phase ripple was ideal toward achieving a linear sensor calibration. When used in an array, the cross-talk was only −39 dB and can be completely eliminated in multiplexed operation. Increasing the operation frequency further for Love wave sensors would limit the

ability to detect larger antigens. The wave penetration into the fluid decreases as $1/\sqrt{\nu}$, where ν is the operating frequency. At 330 MHz, the penetration depth is 31 nm in water.

(a)
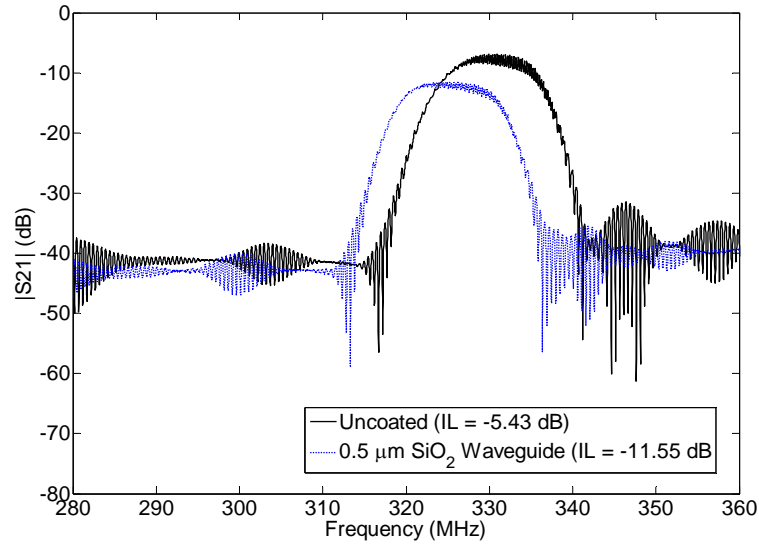
(b)

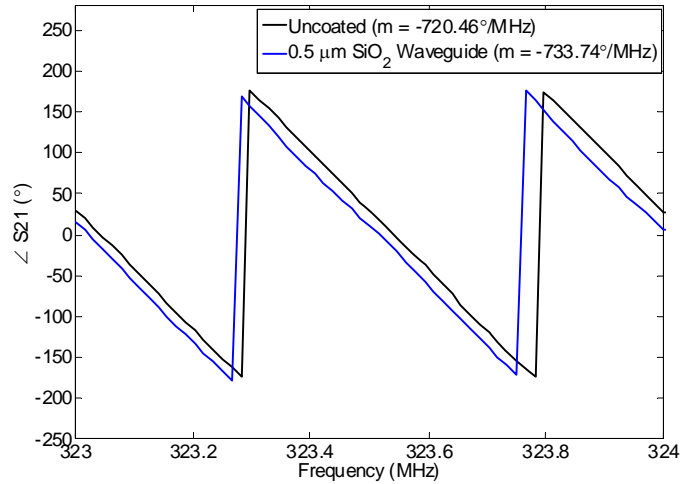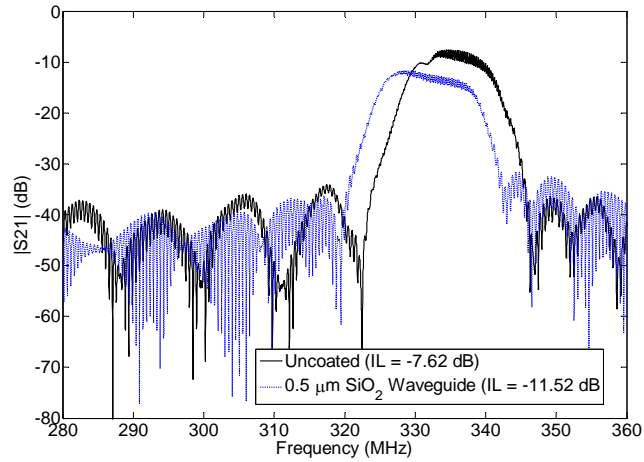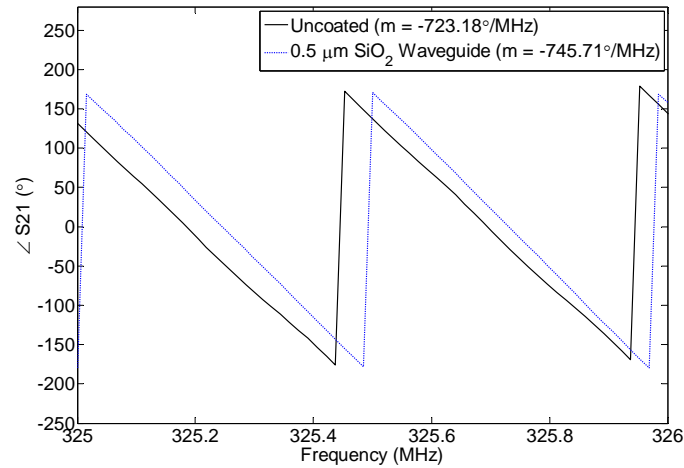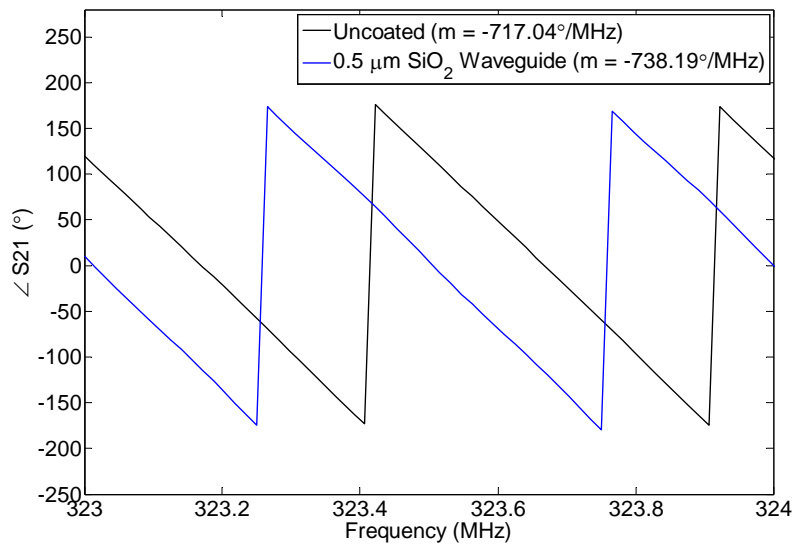**Fig. 23** Measured S21 response of a 330 MHz Love wave sensor in Fig 20c. a) |S21| (dB) and b) phase (°). Increasing the waveguide thickness increased the phase slope.

1.4.8 Non-Destructive Waveguide Analysis

As the waveguide thickness was increased, significant phase slope variation (°/MHz) was observed (Fig. 24). This indicated that even for a highly uniform oxide deposition process (1-2% in thickness) across the wafer; the sensitivity is expected to vary significantly die to die when the waveguide is greater than 2 µm. This problem is slightly mitigated for Love

55

wave sensors operating above 300 MHz, where the optimal thickness waveguide is only a few microns. At the wafer level, a uniform waveguide is exceedingly crucial to achieve sensor reproducibility. The phase slope method was an excellent non-destructive method to assess the sensitivity of the devices prior to biological testing.

$$y = 717.41 + 15.91x + 20.64x^2$$
$$r^2 = 1$$
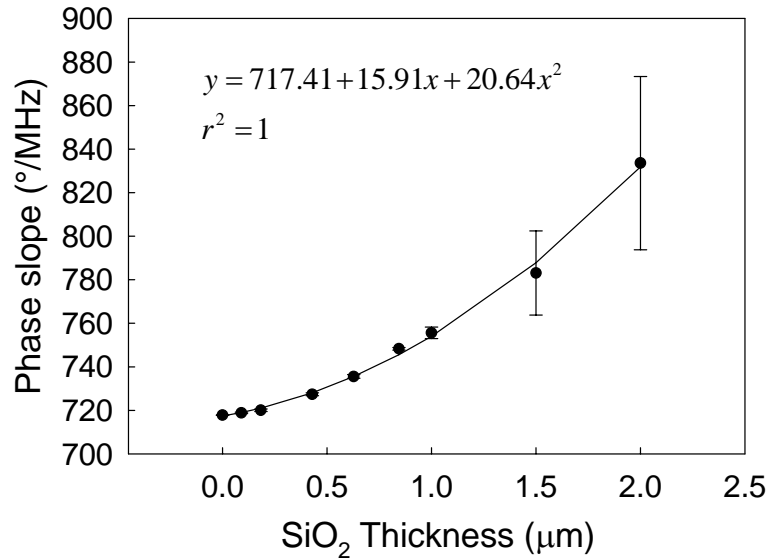
Fig. 24 Phase slope variability as the waveguide thickness increased. The slope of $\angle S21(v)$ ($^\circ$ / MHz) is an indicator of sensitivity. n=8.

1.4.9 Experimentally Determined Mass Sensitivity

The mass sensitivity was measured using the Love wave sensors at waveguide thicknesses of 0.5 µm and 1.0 µm. The results indicate sensitivities of 4.31 ± 0.33 $^\circ$ mm^2 / ng for the 0.5 µm and 7.19 ± 0.74 $^\circ$ mm^2 / ng for the 1 µm waveguides (Fig. 25). This gives a detection limit of 6.7 ± 0.40 pg / mm^2 at 0.01° phase resolution assuming five times the noise level as a conservative value.
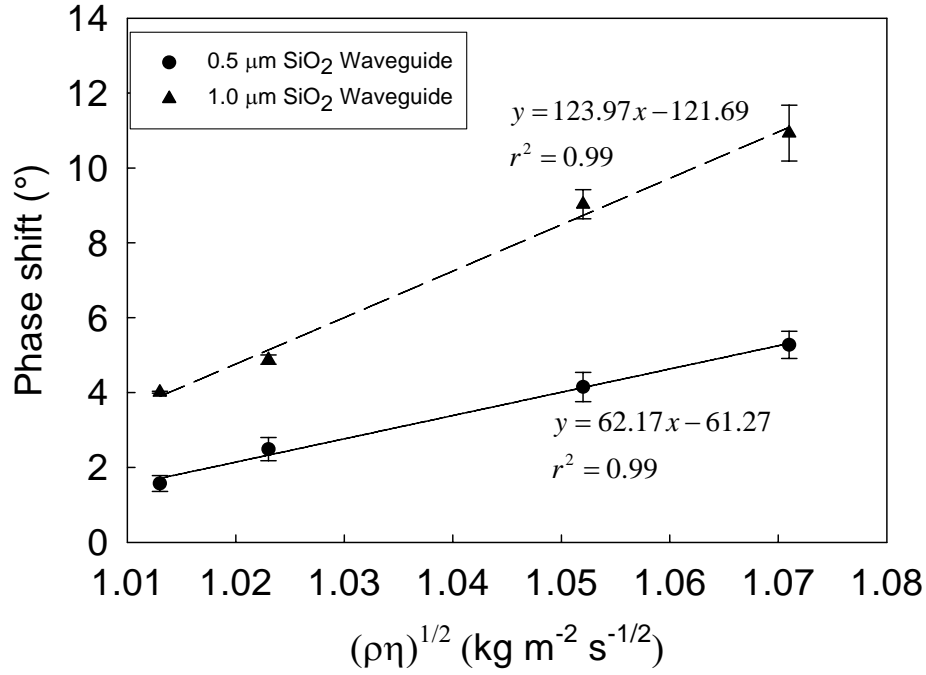
Fig. 25 Phase shift due from glycerin solutions with varying density (ρ) and viscosity (η). − line: 0.5 μm waveguide and -- line:1.0 μm waveguide.

1.4.10 Temperature Compensation

The variation of ambient temperature when using uncompensated piezoelectric crystals shifts the stiffness values in the crystal and causes the propagation delay to change. The thermal coefficient factor (TCF) for 36° YX LTO is -35 ppm/°C. The ST cuts of quartz provide intrinsic thermal compensation but suffer from poor electromechanical coupling and thus high insertion loss. The application of the waveguide can compensate for the thermal variation of 36° YX LTO if the waveguide TCF is positive and applied at the proper thickness. For silicon dioxide, the TCF is +80 ppm/°C with a temperature expansion coefficient of +9 ppm. Computing the temperature coefficient of phase velocity (TCV$_p$) vs. the waveguide thickness is required to determine the thermally compensating waveguide thickness. The TCV$_p$ is related to TCF by

$$TCV_p = \alpha - TCF \tag{1.90}$$

Using the Green's function method to compute the dispersion behavior for silicon dioxide on 36° YX LTO while varying the waveguide thickness at two different temperatures,

$$TCV_p = \frac{1}{V(25°C)} \frac{\partial V_p}{\partial T} \approx \frac{1}{V(25°C)} \frac{V_p(35°C) - V_p(25°C)}{10°C} \tag{1.91}$$

The calculated TCV_p in Fig. 26 shows that a waveguide thickness of 2 µm eliminates thermal variation. This thickness however differs from the optimal theoretical mass sensitivity thickness which was computed to be 3.55 µm.
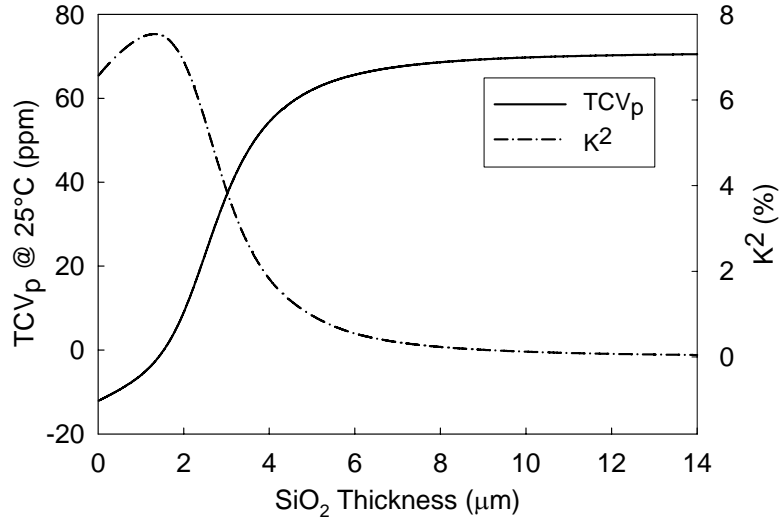
Fig. 26 Theoretical TCV_p vs. silicon dioxide waveguide thickness to achieve thermal compensation

Since the phase shift is the actual parameter measured during detection experiments, the ratio of phase shift to the thermal shift ($\Delta\varphi/\Delta T$) vs. the waveguide thickness approximates the experimental compensation point. In Fig. 27 $\Delta\varphi/\Delta T$ was computed by measuring the phase shift for a given thermal shift once the temperature of the sensor array reached the target value. In this case the value was ~1.5 µm to eliminate thermal shifts in the phase response. The relationship between the phase velocity and phase is not trivial since the phase velocity or time delay maps onto the phase response (0 - 2π).

1.4.11 Multi-Analyte Biodetection

Using three different antibodies covalently attached to the Love wave sensor array, the presence of avidin, BSA, and mouse antigens were detected in real time. The injected concentration for each antigen was 100 ng/ml (5 µl volume). The carrier buffer was 1X PBS pH 7.2. The buffer for each antibody solution was identical to the carrier buffer to minimize

viscosity shifts during injection. The fluid cell dwell time was 24 seconds. In Fig. 28 the phase response is shown for each Love wave sensor. Since the fluid cell was 4 µl, the mean protein diffusion time was about ten seconds, thus the phase response was very rapid. The difference in phase responses was due to variation in binding affinities amongst the antibodies. A separate analysis is required to determine the antibody avidity to each of their intended antigens then compare with the array results.

$$y = -7.50 - 0.388x + 3.33x^2$$
$$r^2 = 0.99$$
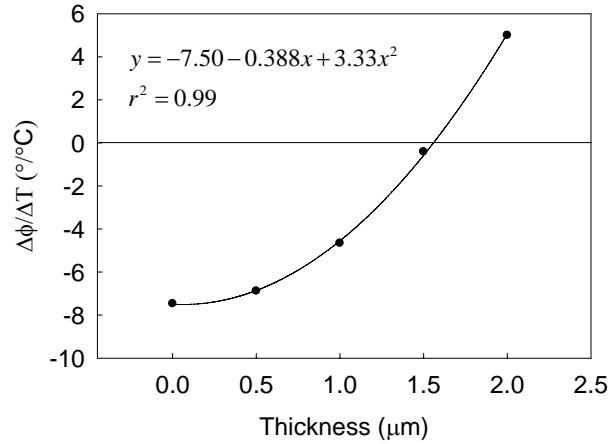
Fig. 27 Measured Δφ/ΔT) vs. silicon dioxide waveguide thickness to achieve thermal compensation. A second order fit was performed to show the behavior in the investigated waveguide thickness range.
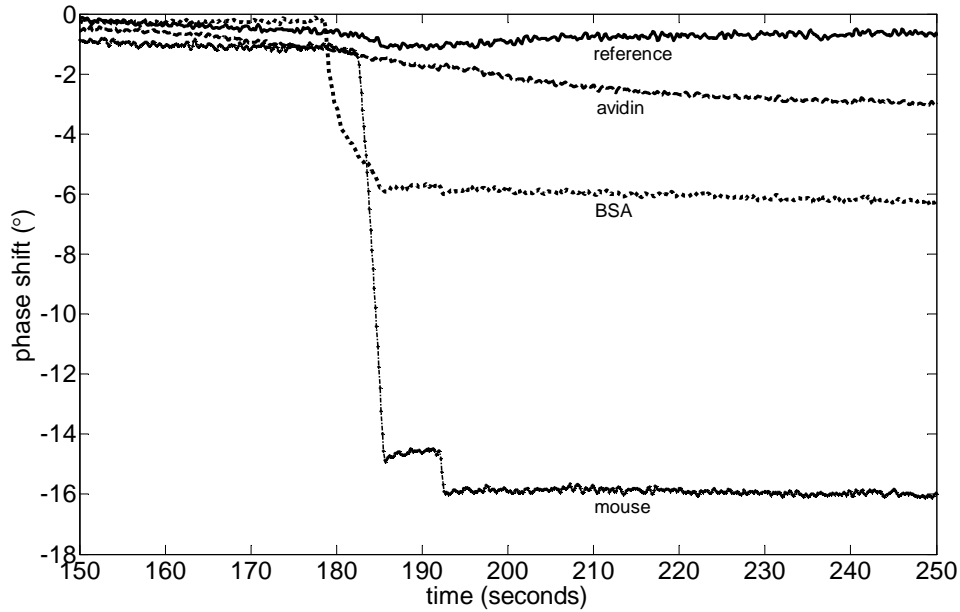
Fig. 28 Multi-analyte biodetection of three antigens in real-time.

59

CONCLUSION

We have developed a suite of modeling codes to simulate and optimize SAW devices. These include Green's function analysis, effective permittivity analysis, 2D and 3D FEM, multilayer isotropic dispersion models, and exact mass sensitivity models. Moreover, new measurement approaches have been presented to assess the sensitivity of the SH-SAW sensors using non-destructive approaches. We have developed an IDT design for high frequency (>300 MHz) Love wave sensors on 36° YX LTO. The IDT design minimized bulk wave interferences, achieved a highly linear phase response (2.8° P-P), and eliminated the need for impedance matching. We present a multi-channel phase detection system that is battery operated. The design was used to create a four channel Love wave array biosensor on a single die. The theoretical sensitivity analysis demonstrated that isotropic models are insufficient to predict sensitivity for 36° YX LTO, despite that the model predicts the optimal waveguide thickness within 10% of the piezoelectric model. We have introduced an analysis method for the nondestructive evaluation of Love wave sensors. The method used the slope of $\angle S21(\nu)$ (° / MHz) to assess the sensitivity and reproducibility of the waveguide. Mass sensitivity results demonstrate the ability to detect at the pg / mm^2 level depending on the noise and resolution of the phase measurement hardware. Finally, we demonstrate the ability to perform multi-analyte detection in real-time.

Piezoelectric Material Properties of Substrates that Support SH and Leaky SH modes

<u>Lithium Tantalate (LTO)</u>

System/Class: Trigonal/3m
Stiffness Tensor (10^{11} N/m^2)

2.33	0.47	0.8	-0.110	0	0
0.47	2.33	0.8	0.110	0	0
0.8	0.8	2.75	0	0	0
-0.110	0.110	0	0.94	0	0
0	0	0	0	0.94	-0.110
0	0	0	0	-0.110	0.93

Piezoelectric Tensor (C/m^2)

0	0	0	0	2.6	-1.6
-1.6	1.6	0	2.6	0	0
0	0	1.9	0	0	0

Permittivity Tensor (10^{-11} F/m)

36.3	0	0
0	36.3	0
0	0	38.1

Density: 4700 kg/m^3

<u>Quartz</u>

System/Class: Trigonal/32
Stiffness Tensor (10^{11} N/m^2)

0.867	0.0699	0.119	-0.179	0	0
0.699	0.867	0.119	0.179	0	0
0.119	0.119	1.72	0	0	0
-0.179	0.179	0	0.579	0	0
0	0	0	0	0.579	-0.179
0	0	0	0	-0.179	0.398

Piezoelectric Tensor (C/m^2)

0.171	-0.171	0	-0.046	0	0
-1.6	1.6	0	2.6	0.046	-0.171
0	0	0	0	0	0

Permittivity Tensor (10^{-11} F/m)

3.920	0	0
0	3.920	0
0	0	4.09

Density: 2650 kg/m^3

Potassium Niobate (KNO)

System/Class: Trigonal/32
Stiffness Tensor (10^{11} N/m^2)

0.867	0.0699	0.119	-0.179	0	0
0.699	0.867	0.119	0.179	0	0
0.119	0.119	1.72	0	0	0
-0.179	0.179	0	0.579	0	0
0	0	0	0	0.579	-0.179
0	0	0	0	-0.179	0.398

Piezoelectric Tensor (C/m^2)

0.171	-0.171	0	-0.046	0	0
-1.6	1.6	0	2.6	0.046	-0.171
0	0	0	0	0	0

Permittivity Tensor (10^{-11} F/m)

3.920	0	0
0	3.920	0
0	0	4.09

Density: 2650 kg/m^3

Langasite (LGS)

System/Class: Trigonal/32
Stiffness Tensor (10^{11} N/m^2)

0.867	0.0699	0.119	-0.179	0	0
0.699	0.867	0.119	0.179	0	0
0.119	0.119	1.72	0	0	0
-0.179	0.179	0	0.579	0	0
0	0	0	0	0.579	-0.179
0	0	0	0	-0.179	0.398

Piezoelectric Tensor (C/m^2)

0.171	-0.171	0	-0.046	0	0
-1.6	1.6	0	2.6	0.046	-0.171
0	0	0	0	0	0

Permittivity Tensor (10^{-11} F/m)

3.920	0	0
0	3.920	0
0	0	4.09

Density: 2650 kg/m^3

Langatite (LGT)

System/Class: Trigonal/32
Stiffness Tensor (10^{11} N/m^2)

0.867	0.0699	0.119	-0.179	0	0
0.699	0.867	0.119	0.179	0	0
0.119	0.119	1.72	0	0	0
-0.179	0.179	0	0.579	0	0
0	0	0	0	0.579	-0.179
0	0	0	0	-0.179	0.398

Piezoelectric Tensor (C/m^2)

0.171	-0.171	0	-0.046	0	0
-1.6	1.6	0	2.6	0.046	-0.171
0	0	0	0	0	0

Permittivity Tensor (10^{-11} F/m)

3.920	0	0
0	3.920	0
0	0	4.09

Density: 2650 kg/m^3

Non-Piezoelectric Material Properties

Silicon Dioxide

System/Class: Isotropic
$C_{11} = 7.85 \cdot 10^{10}$ N/m^2
$C_{44} = 3.12 \cdot 10^{10}$ N/m^2
Density = 2700 kg/m^3
$\varepsilon_r = 3.78$
$\alpha = 3.56$ Np/m @ 1 MHz

Aluminum

System/Class: Isotropic/m3m
$C_{11} = 1.11 \cdot 10^{11}$ N/m^2
$C_{12} = 0.59 \cdot 10^{11}$ N/m^2
$C_{44} = 2.6 \cdot 10^{10}$ N/m^2
Density = 2200 kg/m^3
$\alpha = 0.24$ Np/m @ 1 MHz

Gold

System/Class: Isotropic/m3m
$C_{11} = 1.93 \cdot 10^{11}$ N/m^2
$C_{12} = 1.63 \cdot 10^{11}$ N/m^2
$C_{44} = 4.24 \cdot 10^{10}$ N/m^2
Density = 19300 kg/m^3
$\alpha = 1.9$ Np/m @ 1 MHz

APPENDIX B

Phase and Group Velocity (Lossless Case)

The group velocity (v_g) can be determined exclusively from the phase velocity (v_p) using the expression

$$v_g = \frac{\partial \omega}{\partial k} \tag{1.92}$$

by substituting $k = \omega/v_p$ into (1.92) we have

$$v_p = d\omega \left[d\left(\frac{\omega}{v_p} \right) \right]^{-1} = d\omega \left[\frac{d\omega}{v_p} - \omega \frac{dv_p}{dv_p^2} \right]^{-1} = v_p^2 \left[v_p - \omega \frac{dv_p}{d\omega} \right]^{-1} \tag{1.93}$$

Using $\omega = 2\pi f$, (1.93) can be written as

$$v_g = v_p^2 \left[v_p - (fh) \frac{dv_p}{d(fh)} \right]^{-1} \tag{1.94}$$

where *fh* is the frequency thickness product. When the derivative of v_p with respect to *fh* becomes zero, $v_g = v_p$. In some cases it is convenient to express the group velocity in terms of the normalized thickness (h/λ) by setting $fh = v_p(h/\lambda)$ and substituting into (1.94) we have,

$$v_g = v_p \left[1 - \frac{h/\lambda}{v_p} \frac{d(v_p)}{d(h/\lambda)} \right]^{-1} \tag{1.95}$$

This expression is exact and is ideal for calculating the group velocity from the phase velocity provided that there are no acoustic losses in the layers or the loss is considered negligible. The group velocity can also be calculated using an implicit form of the dispersion relation,

$$v_g = -\frac{\partial \Omega / \partial k}{\partial \Omega / \partial \omega} \tag{1.96}$$

It should be noted that the expression provided by [1] and used by others only approximates (1.95) by Taylor expansion of the bracketed term such that $(1-x)^{-1} \approx 1+x+Ox^2$ and is therefore the Kovacs expression is only accurate to first order.

Perturbation Analysis (Lossless Case)

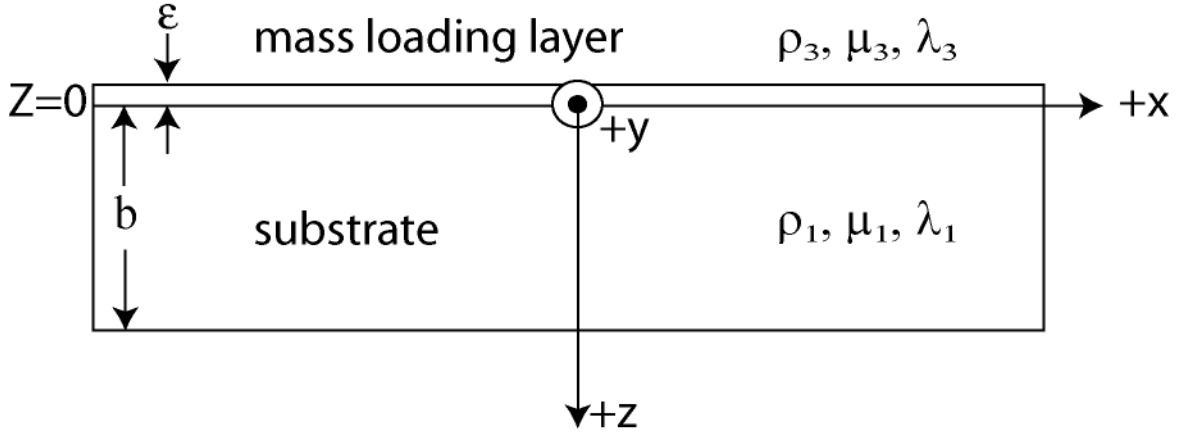**Fig. C.1** Perturbation of the upper mechanical surface (z = 0) by a thin isotropic lossless layer describes by Lamé constants μ_3, λ_3, and density ρ_3.

The task is to compute the perturbation in the velocity ($\Delta V/V$) due to the presence of a thin lossless isotropic layer. The isotropic layer is characterized by a mass density of ρ_3, Lamé constants $\lambda' = c_{44}$ and $\mu' = c_{12}$. The boundary conditions at the upper surface of the mass loading layer are stress-free. The field perturbation is defined as [40]

$$\Delta k_n = k_n' - k_n = \frac{-j\left[-\dot{u}_n^* \cdot T_n' - \dot{u}_n' \cdot T_n^* + \Phi_n^*\left(i\omega D_n'\right) + \Phi_n'\left(i\omega D_n\right)^*\right] \cdot \hat{z}\big|_0^b}{\int_0^b \left[-\dot{u}_n^* \cdot T_n' - \dot{u}_n' \cdot T_n^* + \Phi_n^*\left(i\omega D_n'\right) + \Phi_n'\left(i\omega D_n\right)^*\right] \cdot \hat{x}dz} \tag{1.97}$$

where the perturbed velocity, stress, and electric displacement fields are $\dot{u}_n'$, T_n' and D_n' which must be known to use (1.97). Therefore we seek an approximate expression for the perturbed fields. It must be noted that Eq. (1.97)was derived from the complex reciprocity relation with the requirement that the *unperturbed* material properties are *lossless* [40], however the perturbed system may be *lossy*. Since the perturbation is typically very small the perturbed fields in the denominator may be replaced by the unperturbed fields

$$4P_n = 2\mathbf{Re}\left[\int_0^b \left[-\dot{u}_n^* \cdot T_n' - \dot{u}_n' \cdot T_n^* + \Phi_n^*\left(i\omega D_n'\right) + \Phi_n'\left(i\omega D_n\right)^*\right] \cdot \hat{x}dz\right] \tag{1.98}$$

where P_n is the average unperturbed power flow per unit width along *y*. For mechanical perturbations (1.97) can be simplified by eliminating the electrical boundary perturbation

term $\Phi_n^*\left(i\omega D_n'\right)+\Phi_n'\left(i\omega D_n\right)^*$ and if the perturbation is restricted to only the upper surface such that the second numerator term is zero, giving

$$\Delta k_n = k_n' - k_n = \frac{j\left[-\dot{u}_n^*\cdot T_n'\right]\cdot\hat{z}\big|_{z=0}}{4P_n}$$

(1.99)

The sign change occurs since (1.97) is evaluated at the lower limit of $y=0$. To evaluate (1.99) we assume lossless solutions of the form

$$\dot{u}_i = e^{-jk'r_i}\dot{u}_i'(r_i)e^{j(\omega t - kx)}$$
$$i = x, y, z$$

(1.100)

where k_n' is a pure real propagation constant for the wave. If the perturbation is lossy then k_n' is complex. The acoustic field equations are

$$\nabla \cdot T_{ij} = \hat{x}\left(\frac{\partial}{\partial x}T_{xx} + \frac{\partial}{\partial y}T_{xy} + \frac{\partial}{\partial z}T_{xz}\right)$$
$$+\hat{y}\left(\frac{\partial}{\partial x}T_{yx} + \frac{\partial}{\partial y}T_{yy} + \frac{\partial}{\partial z}T_{yz}\right)$$
$$+\hat{z}\left(\frac{\partial}{\partial x}T_{zx} + \frac{\partial}{\partial y}T_{zy} + \frac{\partial}{\partial z}T_{zz}\right) = \rho\frac{\partial^2 u_i}{\partial t^2} - F_i$$
$$i, j = x, y, z$$

(1.101)

$$\nabla_s \dot{u}_i = \frac{\partial S}{\partial t}$$

(1.102)

Substituting (1.100) (1.101) into with the absence of external forces (*F=0*) gives

$$\frac{\partial}{\partial z}T_{zy}' - jk'T_{xy}' = j\omega\rho_3\dot{u}_y'$$
$$\frac{\partial}{\partial z}T_{zz}' - jk'T_{xz}' = j\omega\rho_3\dot{u}_z'$$
$$\frac{\partial}{\partial z}T_{zx}' - jk'T_{xx}' = j\omega\rho_3\dot{u}_x'$$

(1.103)

Substituting (1.100) into (1.103) gives

$$\frac{\partial \dot{u}'_z}{\partial z} = j\omega\left(\frac{{s'_{11}}^2 - {s'_{12}}^2}{s'_{11}}T'_{zz} + \frac{s'_{12}\left(s'_{11} - s'_{12}\right)}{s'_{11}}T'_{xx}\right) \tag{1.104}$$

$$-jk'\dot{u}'_x = j\omega\left(\frac{s'_{12}\left(s'_{11} - s'_{12}\right)}{s'_{11}}T'_{zz} + \frac{{s'_{11}}^2 - {s'_{12}}^2}{s'_{11}}T'_{xx}\right) \tag{1.105}$$

$$\frac{\partial v'_x}{\partial z} - jk\dot{u}'_z = j\omega s'_{44}T'_{zx} \tag{1.106}$$

$$-jk\dot{u}'_y = j\omega s'_{44}T'_{yx} \tag{1.107}$$

$$\frac{\partial \dot{u}'_y}{\partial z} = j\omega s'_{44}T'_{zy} \tag{1.108}$$

To obtain an approximate solution, the fields are expanded as a Taylor series

$$\dot{u}'(z) = \dot{u}^{(0)} + \dot{u}^{(1)}(z+\varepsilon) + \dot{u}^{(2)}\left(z+\varepsilon\right)^2 + \dots$$
$$T'(z) = T^{(0)} + T^{(1)}(z+\varepsilon) + T^{(2)}\left(z+\varepsilon\right)^2 + \dots \tag{1.109}$$

The boundary at $y = -\varepsilon$ is a stress-free boundary in Fig. C.1 requires that

$$T^0 \cdot \hat{z} = 0 \tag{1.110}$$

and (1.103) becomes

$$T^{(1)}_{zy} - jk'T^{(0)}_{xy} = j\omega\rho_3\dot{u}^{(0)}_y$$
$$T^{(1)}_{zz} = j\omega\rho_3\dot{u}^{(0)}_z$$
$$T^{(1)}_{xz} - jk'T^{(0)}_{xx} = j\omega\rho_3\dot{u}^{(0)}_x$$
$$-jk'\dot{u}^{(0)}_x = j\omega\frac{{s'_{11}}^2 - {s'_{12}}^2}{s'_{11}}T^{(0)}_{xx} \tag{1.111}$$
$$-jk'\dot{u}^{(0)}_y = j\omega s'_{44}T^{(0)}_{yx}$$

Solving for $T^{(1)} \cdot \hat{z}$ as a function of $v^{(0)}$ gives

$$T_{xx}^{(1)} \cdot \hat{z} = h \left(\frac{-j\omega k' \dot{u}_x^{(0)}}{j\omega} \frac{s_{11}'}{s_{11}'^2 - s_{12}'^2} \right) = j\omega h \left[\rho_3 - \frac{k'^2}{\omega^2} \left(\frac{s_{11}'}{s_{11}'^2 - s_{12}'^2} \right) \right] \dot{u}_x^{(0)}$$

$$T_{zz}^{(1)} \cdot \hat{z} = j\omega \rho_3 h \dot{u}_z^{(0)}$$

$$T_{zy}^{(1)} \cdot \hat{z} = h \left(j\omega \rho_3 \dot{u}_y^{(0)} + jk' \left(\frac{-jk' \dot{u}_y^{(0)}}{j\omega s_{44}'} \right) \right) = j\omega h \left[\rho_3 - \frac{k'^2}{\omega^2} \frac{1}{s_{44}'} \right] \dot{u}_y^{(0)}$$

(1.112)

For an isotropic material the compliance is related to the stiffness by

$$s_{11} = \frac{c_{11} + c_{12}}{(c_{11} - c_{12})(c_{11} + 2c_{12})}$$

$$s_{44} = \frac{1}{c_{44}}$$

(1.113)

$$s_{12} = s_{11} = \frac{s_{44}}{2}$$

Using the following definitions and relations derived from (1.113) we have

$$\frac{1}{s_{44}} = \mu$$

$$c_{12} = \lambda$$

(1.114)

$$\frac{s_{11}'}{s_{11}'^2 - s_{12}'^2} = \frac{4(\lambda + \mu)\mu}{\lambda + 2\mu}$$

and (1.112) can be written as

$$T_{xx}^{(1)} \cdot \hat{z} = j\omega h \left[\rho_3 - \frac{1}{(\omega/k')^2} \left(\frac{4(\lambda_3 + \mu_3)\mu_3}{\lambda_3 + 2\mu_3} \right) \right] \dot{u}_x^{(0)}$$

$$T_{zz}^{(1)} \cdot \hat{z} = j\omega \rho_3 h \dot{u}_z^{(0)}$$

(1.115)

$$T_{zy}^{(1)} \cdot \hat{z} = j\omega h \left[\rho_3 - \frac{\mu_3}{(\omega/k')^2} \right] \dot{u}_y^{(0)}$$

Inserting these into (1.99) gives

$$-\frac{\Delta V}{V} = \frac{\Delta k}{k} = \frac{(\omega/k')h}{4P_n} \left[\left(\rho_3 - \frac{\mu_3}{(\omega/k')^2} \right) |\dot{u}_y|^2 + \rho_3 |\dot{u}_z|^2 + \left(\rho_3 - \frac{1}{(\omega/k')^2} \left(\frac{4(\lambda_3 + \mu_3)\mu_3}{\lambda_3 + 2\mu_3} \right) \right) |\dot{u}_x|^2 \right]$$

(1.116)

$$V = \omega/k'$$

Perturbation Analysis (Lossy Case)

If the unperturbed system is lossy then the phase velocity V is complex and (1.116) requires that $k' = \alpha + j\beta$, however this means that there are now cutoff or non-propagating modes. The average power flow now reflects the lossy waveguide with a new orthogonal relation for complex propagation constants as compared to (1.98). The complex wave propagation k require a new formulation of the dispersion relationship to account for the acoustic losses in the layers.

REFERENCES

[1]   G. Kovacs, G. W. Lubking, M. J. Vellekoop, and A. Venema, "Love waves for (bio)chemical sensing in liquids," *Ultrason. Symp.,* pp. 281-285, 1992.

[2]   G. Harding, J. Du, P. Dencher, D. Barnett, and E. Howe, "Love wave acoustic immunosensor operating in liquid," *Sensors Actuators A,* vol. 61, pp. 279-286, 1997.

[3]   O. Tamarin, S. Comeau, C. Déjous, D. Moynet, D. Rebière, J. Bezian, and J. Pistré, "Real time device for biosensing: design of a bacteriophage model using love acoustic waves," *Biosensors and Bioelectronics,* vol. 18, pp. 755-763, 2003.

[4]   D. W. Branch and S. M. Brozik, "Low-Level Detection of a Bacillus Anthracis Simulant using Love-Wave Biosensors on 36° YX LiTaO3," *Biosensors and Bioelectronics,* vol. accepted, p. submitted, 2003.

[5]   Z. Wang and J. D. N. Cheeke, "Sensitivity analysis for love mode acoustic gravimetric sensors," *Appl. Phys. Lett.,* vol. 64, pp. 2940-2942, 1994.

[6]   E. Gizeli, A. C. Stevenson, N. J. Goddard, and C. R. Lowe, "A novel Love-plate acoustic sensor utilizing polymer overlayers," *IEEE Trans. Ultrason. Ferroelect. Freq. Contr.,* vol. 39, pp. 657-659, 1992 1992.

[7]   F. Herrmann, M. Weihnacht, and S. Büttgenbach, "Properties of sensors based on shear-horizontal surafce acoustic waves in $LiTaO_3/SiO_2$ and quartz/SiO_2 structures," *IEEE Trans. Ultrason. Ferroelect. Freq. Contr.,* vol. 48, pp. 268-273, 2001.

[8]   D. A. Powell, K. Kalantar-zadeh, S. Ippolito, and W. Wlodarski, "A layered SAW device based on ZnO/LiTaO3 for liquid media sensing applications," *IEEE Ultrason. Symp. Proc.,* pp. 493-496, 2002.

[9]   L. Rayleigh, "On Waves Propagated along the Plane Surface of an Elastic Solid," *Proc. London Math Soc.,* vol. s1-s17, pp. 4-11, 1885.

[10]   J.-i. Kushibiki, I. Takanaga, M. Arakawa, and T. Sannomiya, "Accurate measurements of the acoustical physical constants of $LiNbO_3$ and $LiTaO_3$ single crystals," *IEEE Trans. Ultrason. Ferroelect. Freq. Contr.,* vol. 46, pp. 1315-1323, 1999.

[11]   T. B. Pollard, J. F. Vetelino, and M. P. d. Cunha, "Pure SH SAW on single crystal $KNbO_3$ for liquid sensor applications," *IEEE Ultrason. Symp. Proc.,* pp. 1125-1128, 2003.

[12]   C. K. Campbell, *Surface Acoustic Wave Devices for Mobile and Wireless Communications (Applications of Modern Acoustics*. New York: Academic Press, 1998.

[13]   M. P. d. Cunha and D. C. Malocha, "Pure Shear Horizontal SAW On Langatate," *IEEE 2000 International Ultrasonics Symposium Proceedings,* pp. 231-234, 2000.

[14]   M. P. d. Cunha and D. C. Malocha, "Experimental and predicted SAW temperature behavior of langatate," *IEEE Ultrason. Symp. Proc.*

[15]   E. Berkenpas, S. Bitla, P. Millard, and M. P. d. Cunha, "Pure shear horizontal SAW biosensor on Langasite," *IEEE Trans. Ultrason. Ferro. Freq Cntrl.,* vol. 51, pp. 1404-1411, 2004.

[16]   K. A. Ingebrigtsen, "Surface-acoustic waves in piezoelectrics," *J. Appl. Phys.,* vol. 40, pp. 2681-2686, 1969.

[17]   J. J. Campbell and W. R. Jones, "A method for estimating optimal crystal cuts and propagation directions for excitation of piezoelectric surface waves," *IEEE Trans. Sonics Ultrason.,* vol. 15, pp. 209-217, 1968.

[18] E. L. Adler, "SAW and pseudo-SAW properties using matrix methods," *IEEE Trans. Ultrason. Ferroelectr. Freq. Cntrl,* vol. 41, pp. 876-882, 1994.

[19] R. C. Peach, "A general Green's function analysis for SAW devices," *IEEE Ultrason. Symp. Proc.,* pp. 221-225, 1995.

[20] V. P. Plessky and T. Thorvaldsson, "Periodic Green's functions analysis of SAW and leaky propagation in a periodic system of electrodes on a piezoelectric crystal," *IEEE Trans. Ultrason., Ferroelectr. Freq. Cntrl.,* vol. 42, pp. 280-293, 1995.

[21] J. J. Campbell and W. R. Jones, "Propagation of surface waves at the boundary between a piezoelectric crystal and a fluid medium," *IEEE Trans. Sonic and Ultrason.,* vol. 17, pp. 71-76, 1970.

[22] G. W. Farnell, "Symmetry considerations for elastic layer modes propagating in anisotropic piezoelectric crystals," *IEEE Trans. Son. Ultrason.,* vol. 17, pp. 229-238, 1970.

[23] D. Qiao, W. Liu, and P. M. Smith, "General Green's functions for SAW device analysis," *IEEE Trans. Ultrason. Ferroelectr. Freq. Cntrl,* vol. 46, pp. 1242-1253, 1999.

[24] B. Jakoby and M. J. Vellekoop, "Analysis and optimization of love wave liquid sensors," *IEEE Trans. Ultrason. Ferroelect. Freq. Contr.,* vol. 45, pp. 1293-1302, 1998.

[25] R. Ro, S.-Y. Chang, R.-C. Hwang, and D. H. Lee, "Identification of ionic solutions using a SAW liquid sensor," *Proc. Natl. Counc. ROC(A),* vol. 23, pp. 810-815, 1999.

[26] T. Yamazaki, J. Kondoh, Y. Matsui, and S. Shiokawa, "Estimation of components and concentration in mixture solutions of electrolytes using a liquid flow system with SH-SAW sensor," *Sensors Actuators A,* vol. 83, pp. 34-39, 2000.

[27] R. Ro, S. K. Yang, H. Y. Lee, and C. Y. Shen, "Effects of conducting liquid loadings on propagation characteristics of surface acoustic waves," *Proc. Natl. Sci. Counc. ROC(A),* vol. 25, pp. 131-136, 2001.

[28] R. F. Harrington, *Field computation by moment methods*. New York: IEEE Press, 1993.

[29] R. F. Milsom, N. H. C. Reilly, and M. Redwood, "Analysis of generation and detection of surface and bulk acoustic waves by interdigital transducers," *IEEE Trans. Son. and Ultrason.,* vol. 24, 1977.

[30] D. P. Morgan, *Surface-wave devices for signal processing*. Amsterdam: Elsevier, 1985.

[31] A. R. Baghai-Wadji, O. Männer, and R. Ganβ-Punchstein, "Analysis and measurement of transducer end radiation in SAW filters on strongly coupling substrates," *IEEE Trans. Microwave Theor. and Tech.,* vol. 37, pp. 150-158, 1989.

[32] M. Politi, G. Macchiarella, and G. B. Stracca, "Fast computation of static capacitance for periodic SAW transducers," *IEEE Trans. Ultrason. Ferro. Freq Cntrl.,* vol. 35, pp. 708-710, 1988.

[33] C.-J. Chen, "Finite-cell-gap corrections to the capacitance analysis of liquid crystal displays with periodic interdigital electrodes," *J. Appl. Physics,* vol. 87, pp. 5-9, 2000.

[34] S. Datta, B. J. Hunsinger, and D. C. Malocha, "Element factor for periodic transducers," *IEEE Trans. Sonics Ultrason.,* vol. 27, pp. 42-44, 1980.

[35]   S. W. Wenzel and R. M. White, "Analytic comparison of the sensitivities of bulk-wave, surface-wave, and flexural plate-wave ultrasonic gravimetric sensors," *Appl. Phys. Lett.,* vol. 54, pp. 1976-1978, 15 May 1989.

[36]   A. Malavé, U. Schlecht, T. M. A.Gronewold, M. Perpeet, and M. Tewes, "Lithium tantalate surface acoustic wave sensors for bio-analytical applications," *IEEE Sensors,* pp. 604-607, 2006.

[37]   A. W. Warner, M. Onoe, and G. A. Coquin, "Determination of elastic and piezoelectric constants for crystals in class (3m)," *J. Acoustical Soc. Amer.,* vol. 42, pp. 1223-1231, 1967.

[38]   C. S. Hartmann and B. P. Abbott, "Overview of design challenges for single phase unidirectional SAW filters," *Ultrason. Symp. Proc.,* pp. 79-89, 1989.

[39]   Y. Shui, J. M. Lin, H. Wu, N. Wang, and H. Chen, "Optimization of single-phase, unidirectional transducers using three fingers per period," *IEEE Trans. Ultrason. Ferro. Freq Cntrl.,* vol. 49, pp. 1617-1621, 2002.

[40]   B. A. Auld, *Acoustic fields and waves in solids*, 2nd ed. ed. Malabar: Krieger Publishing Co., 1990.

DISTRIBUTION LIST

10	MS 1425	Darren W. Branch, 1714
1	MS 1425	Thayne Edwards, 1714
1	MS 1425	Steve Casalnuovo, 1714
1	MS 0892	Richard Cernosek, 1744
1	MS 0892	Susan Brozik, 1714
1	MS 1304	Dale Huber, 1132
1	MS 0899	Technical Library, 9536 (electronic copy)